

1 **An assessment of land energy balance over East Asia from**  
2 **multiple lines of evidence and the roles of Tibet Plateau,**  
3 **aerosols, and clouds**

4  
5 Qiuyan Wang<sup>1,2,6</sup>, Hua Zhang<sup>1,2</sup>, Su Yang<sup>3</sup>, Qi Chen<sup>2</sup>, Xixun Zhou<sup>2</sup>, Bing Xie<sup>4</sup>, Yuying  
6 Wang<sup>1</sup>, Guangyu Shi<sup>1,5</sup>, Martin Wild<sup>6</sup>

7  
8 <sup>1</sup> Collaborative Innovation Center on Forecast and Evaluation of Meteorological Disasters, Nanjing University  
9 of Information Science and Technology, Nanjing 210044, China

10 <sup>2</sup> State Key Laboratory of Severe Weather, Chinese Academy of Meteorological Sciences, Beijing 100081,  
11 China

12 <sup>3</sup> National Meteorological Information Center, China Meteorological Administration, Beijing 100081, China

13 <sup>4</sup> Laboratory for Climate Studies of China Meteorological Administration, National Climate Center, Beijing  
14 100081, China

15 <sup>5</sup> State Key Laboratory of Numerical Modeling for Atmospheric Sciences and Geophysical Fluid Dynamics,  
16 Institute of Atmospheric Physics, Chinese Academy of Sciences, Beijing 100029, China

17 <sup>6</sup> Institute for Atmospheric and Climate Science, ETH Zurich, 8092 Zurich, Switzerland

18

19 *Corresponding to:* Hua Zhang (huazhang@cma.gov.cn)

20

21 **Abstract.** With high emissions of aerosols and the known world’s “Third Pole” of the Tibet Plateau (TP) in  
22 East Asia, knowledge on the energy budget over this region is widely concerned. This study first attempts  
23 to estimate the present-day land energy balance over East Asia by combining surface and satellite  
24 observations, as well as the atmospheric reanalysis and Coupled Model Intercomparison Project phase 6  
25 (CMIP6) simulations. Compared to the global land budget, a substantially larger fraction of atmospheric  
26 shortwave radiation of 5.2% is reflected, highly associated with the higher aerosol loadings and more clouds  
27 over East Asian land. While a slightly smaller fraction of atmospheric shortwave absorption of 0.6% is  
28 unexpectedly estimated, possibly related to the lower water vapor content effects due to the thinner air over  
29 the TP to overcompensate for the aerosol and cloud effects over East Asian land. The weaker greenhouse  
30 effect and fewer low clouds due to the TP are very likely the causes for the smaller fraction of East Asian-  
31 land surface downward longwave radiation. Hence, high aerosol loadings, clouds, and the TP over East Asia  
32 play vital roles in the shortwave budgets, while the TP is responsible for the longwave budgets during this  
33 regional energy budget assessment. The further obtained cloud radiative effects suggest that the presence of  
34 clouds results in a larger cooling effect on the climate system over East Asian land than that over globe. This  
35 study provides a perspective to understand fully the roles of potential factors in influencing the different  
36 energy budget assessments over regions.

37

## 38 **1. Introduction**

39 Current patterns of Earth’s weather and climate are largely determined by the spatiotemporal  
40 distributions of energy exchanges between the surface, atmosphere, and space. Theoretically, the outgoing  
41 longwave radiation (OLR) is balanced by the incoming and reflected solar radiation at the top of the  
42 atmosphere (TOA) to produce an equilibrium climate. The incoming solar radiation can be scattered by  
43 clouds and aerosols or absorbed by the intermediary atmosphere, thereby contributing to the diverse energy  
44 transformation at the surface (Trenberth et al., 2009; Wild et al., 2013a). The Earth’s surface energy balance  
45 is of particular significance because it is the key driver of atmospheric and oceanic circulations, hydrological  
46 cycles, and various surface processes (Wild et al., 2008; Mercado et al., 2009; Wild et al., 2013a; L’Ecuyer  
47 et al., 2015). Anthropogenic influences on climate change are driven by the uneven distribution of the TOA  
48 net radiation caused by forcings perturbed by variations of the atmospheric composition of greenhouse gases  
49 and aerosols as well as aerosol-cloud interactions (Trenberth et al., 2009; Stephens et al., 2012; Wild et al.,  
50 2013a; Trenberth et al., 2014; L’Ecuyer et al., 2015; Wild et al., 2019).

51 Many efforts have been made to quantify the magnitudes of different radiative components or energy  
52 budgets in the climate system over a range of time-space scales, such as on global scales (Lin et al., 2008;  
53 Trenberth et al., 2009; Stephens et al., 2012; Wild et al., 2013b; Wild et al., 2015; L’Ecuyer et al., 2015;  
54 Wild et al., 2019; Wild, 2020), over land and ocean domains or the energy transport between them (Fasullo  
55 and Trenberth, 2008a, b; Trenberth et al., 2009; Wild et al., 2015; L’Ecuyer et al., 2015), over the Arctic  
56 (Previdi et al., 2015; Christensen et al., 2016), and over individual continents and ocean basins (L’Ecuyer et  
57 al., 2015; Kim and Lee, 2018; Thomas et al., 2020). The energy balance at the TOA can be accurately

58 monitored by satellites from the most advanced Clouds and the Earth's Radiant Energy System (CERES)  
59 Energy Balanced and Filled (EBAF) data product (Loeb et al., 2018), while considerably larger uncertainties  
60 appear at the surface fluxes owing to weaker observational constraints (Raschke et al., 2016; Kato et al.,  
61 2018; Huang et al., 2019). These assessments mostly build upon complementary approaches from a  
62 combination of space and surface observations, climate models, and reanalyses. To date, the discrepancies  
63 of independent global mean surface radiative fluxes have estimated to be within a few  $\text{W m}^{-2}$  (Wild, 2017a,  
64 b), enabling the accurate quantification of global surface budgets. In addition, the surface radiative  
65 components simulated by various climate models vary substantially in a range of around 10–20  $\text{W m}^{-2}$  on  
66 global scales, but exhibit greater inter-model discrepancies on regional scales (Li et al., 2013; Wild et al.,  
67 2013a; Boeke and Taylor, 2016; Wild et al., 2015; Wild, 2017a, b, 2020). Existing challenges on the surface  
68 energy estimates include considerable uncertainties from surface albedo and skin temperature, as well as the  
69 partitioning of surface net radiation into sensible and latent heat (SH; LH) (Wild, 2017a, b).

70 Due to the large population and the largest emission source of aerosols and their precursors, East Asia,  
71 especially China, has long been a hotspot in climate change research. Aerosols can interact with radiation  
72 directly by scattering and absorbing solar/thermal radiation (Ghan et al., 2012) and indirectly by modifying  
73 cloud microphysical properties and lifetimes (Li et al., 2011), thereby influencing Earth's radiation balance.  
74 As the world's largest and highest plateau, the Tibet Plateau (TP) covers nearly one third of the East Asian  
75 land area, significantly affecting the atmospheric circulation, energy budget, and water cycles of climate  
76 system through its orographic and thermal effects (Liu et al., 2007; Xu et al., 2008a, b; Wu et al., 2015).  
77 Deeper insights into the energy budget differences over East Asian and global land under the background of  
78 high aerosol emissions and the role of the TP in East Asia are of the meaningful and essential attempts.  
79 Moreover, clouds play a key role in modulating global and regional energy budgets and hydrological cycles  
80 through increasing the reflected solar radiation and also the downward thermal radiation, leading to a cooling  
81 and warming of climate system (Stephens, 2005; Wild et al., 2013a; Li et al., 2015; H. Wang et al., 2021).  
82 Therefore, our emphasis in this study is on the regional characterization of the East Asian energy balance  
83 under both all-sky and clear-sky conditions based on a combination of surface observations, satellite-derived  
84 products, reanalysis, and Coupled Model Intercomparison Project phase 6 (CMIP6) models. The cloud  
85 influence on the radiative energy budgets at the TOA, within the atmosphere, and at the surface is further  
86 quantified over this region. Section 2 introduces the different data sources used in this study, including  
87 surface and satellite observations, climate models, and reanalysis. Sections 3 and 4 provide detailed analyses  
88 of the all-sky and clear-sky estimates of the energy balance components. The inferred cloud radiative effects  
89 (CREs) at the TOA, within the atmosphere, and at the surface are presented in Section 5. Summary and  
90 conclusions are given in Section 6. The present-day in this study represents years of 2010–2014, which  
91 corresponds to the last five years of the historical simulations in CMIP6 climate models. East Asian land as  
92 considered in this study consists of five countries, including China, Japan, South and North Korea, as well  
93 as Mongolia.

94

## 95 2. Data sources

### 96 2.1. Surface observations

97 Considering the efforts to diminish the inhomogeneities in the measurement of ground-based surface  
98 (downward) solar radiation (SSR) (Tang et al., 2011; Wang, 2014; Wang et al., 2015; Wang and Wild, 2016;  
99 He et al., 2018; Yang et al., 2018, 2019) and the large amount of observational stations over China, the  
100 homogenized monthly all-sky and clear-sky SSR datasets from the China Meteorological Administration  
101 (CMA) National Meteorological Information Center (NMIC) are used in this study (<http://data.cma.cn/en/>)  
102 (Yang et al., 2018, 2019). In this dataset, the clear-sky condition at observational sites is defined based on  
103 the measured cloud fraction per day of no more than 15% (Yang et al., 2018). Taking clear-sky data (with  
104 relatively complex missing months compared to the all-sky dataset) as an example, sites with more than one  
105 year of  $> 2$  missing months were deleted to ensure  $\geq 4$  years of available data during the period 2010-2014,  
106 then the spline interpolation was performed on the missing months of the selected sites. As a consequence,  
107 99 and 76 sites are available for the all-sky and clear-sky studies, respectively. Besides, to further explore  
108 the anthropogenic influence on SSR, 84 (62) urban and 15 (14) rural stations for all-sky (clear-sky)  
109 conditions are defined according to the administrative divisions of China (Wang et al., 2017).

110 For the remaining East Asian sites, we use the monthly Global Energy Balance Archive (GEBA) dataset  
111 (<http://www.geba.ethz.ch>) (Wild et al., 2017), which contains a worldwide widespread distribution of  
112 monthly data from many sources, e.g., from the World Radiation Data Center (WRDC), the Baseline Surface  
113 Radiation Network (BSRN), etc. Among these data sources, the BSRN dataset has a much higher precision  
114 and temporal resolution (up to 1 min) compared to the GEBA, but its site number is very limited over East  
115 Asia (only a few sites located in Japan and one site in Xianghe, China, but with no data available during this  
116 study period). Moreover, the relative random error of the monthly SSR from the GEBA data evaluated by  
117 Gilgen et al. (1998) is 5%.

118 In order to retain as many sites as possible during the study period, we widen the selection criterion of  
119 the GEBA data, i.e., sites with data  $\geq 4$  years and missing months  $\leq 3$ . Eventually, 8, 2, 4, and 14 sites are  
120 selected from GEBA in China, Mongolia, South and North Korea, and Japan, respectively. Especially,  
121 among the 14 sites in Japan, five pairs of the duplicate sites are obtained from the WRDC and BSRN sources,  
122 respectively, and the left 4 sites are only from the WRDC (9 sites available). For China, only one site from  
123 Hongkong out of 8 GEBA sites is not repetitive from the above-mentioned CMA sites (1 site available).  
124 Therefore, 16 out of 28 GEBA sites are available under all-sky conditions (including 15 sites over regions  
125 outside China and 1 site over Hongkong, China) by taking the average of these duplicate sites in Japan  
126 instead, while the clear-sky reference sites are obtained from the interpolated CERES EBAF clear-sky  
127 estimates at the GEBA sites (also 16 sites) due to the limited numbers of observational sites over these  
128 regions. Additionally, we regard four island sites in Japan as rural stations (not shown in the figures), while  
129 the sites in Mongolia as well as South and North Korea are all urban sites.

130 As shown in Fig. S1, there are 99 (rural/total: 15/99) and 16 (rural/total: 4/16) sites from the CMA and  
131 GEBA available under all-sky conditions, respectively, whereas 76 (rural/total: 14/99) and 16 (from the  
132 CERES-interpolated data at the 16 GEBA sites) sites are considered for clear-sky conditions, respectively.  
133 More detailed station information is given in Table S1.

134

## 135 2.2. Satellite observation

136 Owing to the excellent temporal and spatial coverage of satellite instruments, CERES data products are  
137 widely used to track variations of Earth's energy budgets. The newly released CERES EBAF Edition 4.1  
138 with a monthly  $1^\circ \times 1^\circ$  latitude-longitude resolution is used in this study (<https://ceres.larc.nasa.gov/data/>). In  
139 this dataset, the TOA radiation components are adjusted within their uncertainty ranges based on the  
140 independent observational ocean estimates of global heating rate (Loeb et al., 2018). Unlike the directly  
141 measured TOA energy budget, the EBAF-surface energy fluxes are calculated by the cloud and aerosol  
142 properties from satellite-derived products as well as the atmospheric profiles from reanalysis, with a lower  
143 accuracy than their TOA counterparts (Kato et al., 2018). The uncertainty ranges in  $1^\circ \times 1^\circ$  regional monthly  
144 all-sky and clear-sky longwave (LW) and shortwave (SW) radiation fluxes at the TOA are also documented  
145 by Loeb et al. (2018).

146

## 147 2.3. Climate models and reanalysis

148 Data from 40 CMIP6 climate models are used for the analyses in this study with their model  
149 abbreviations, modeling groups, and resolutions in Table S2. A detailed description of the modeling groups  
150 participating in CMIP6 is provided at <https://pcmdi.llnl.gov/CMIP6/>. The CMIP6 model-calculated radiation  
151 fluxes under investigation for this study include energy budgets under both all-sky and clear-sky conditions  
152 from 'historical all forcings' experiments covering the period 2010-2014. In these historical simulations,  
153 both natural (e.g., solar variability and volcanic aerosols) and anthropogenic (e.g., greenhouse gases, aerosols,  
154 and land use) forcings are considered to reproduce the climate change and evolution since preindustrial times  
155 as accurately as possible (Eyring et al., 2016). Only the first ensemble member of each model is selected for  
156 the analysis and the model numbers vary slightly among different available energy components.

157 In the long history of the European Center for Medium-range Weather Forecast (ECMWF), ERA5 is  
158 the fifth generation product. It is a comprehensive reanalysis from 1979 (soon be backdated to 1950) to near  
159 real time, which assimilates as many observations as possible in the upper air and near surface  
160 (<https://cds.climate.copernicus.eu/>). Monthly means of the radiative components from ERA5 are used in this  
161 study with a resolution of  $0.25^\circ \times 0.25^\circ$  (regridDED to  $1^\circ \times 1^\circ$ ). Compared to previous reanalyses (such as ERA-  
162 Interim), a major strength of ERA5 is the much higher temporal and spatial resolutions, as well as a larger  
163 number of vertical levels (Hersbach et al., 2020). Several independent studies have evaluated the  
164 performance of ERA5 since its release. For example, excellent closure of the Arctic energy budget based on  
165 ERA5 atmospheric data has been assessed by Mayer et al. (2019). The representation of surface irradiance

166 of ERA5 has been compared with other reanalyses and with ground and satellite observations (Trollet et al.,  
167 2018; Urraca et al., 2018). Specifically, Trollet et al. (2018) found that the surface solar irradiance over the  
168 tropical Atlantic Ocean from ERA5 exhibits fewer biases than the second version of the Modern-Era  
169 Retrospective Analysis for Research and Applications (MERRA-2). Urraca et al. (2018) reported that ERA5  
170 can be a valid alternative for satellite-derived products in terms of surface irradiance in most inland stations  
171 compared to ERA-Interim or MERRA-2.

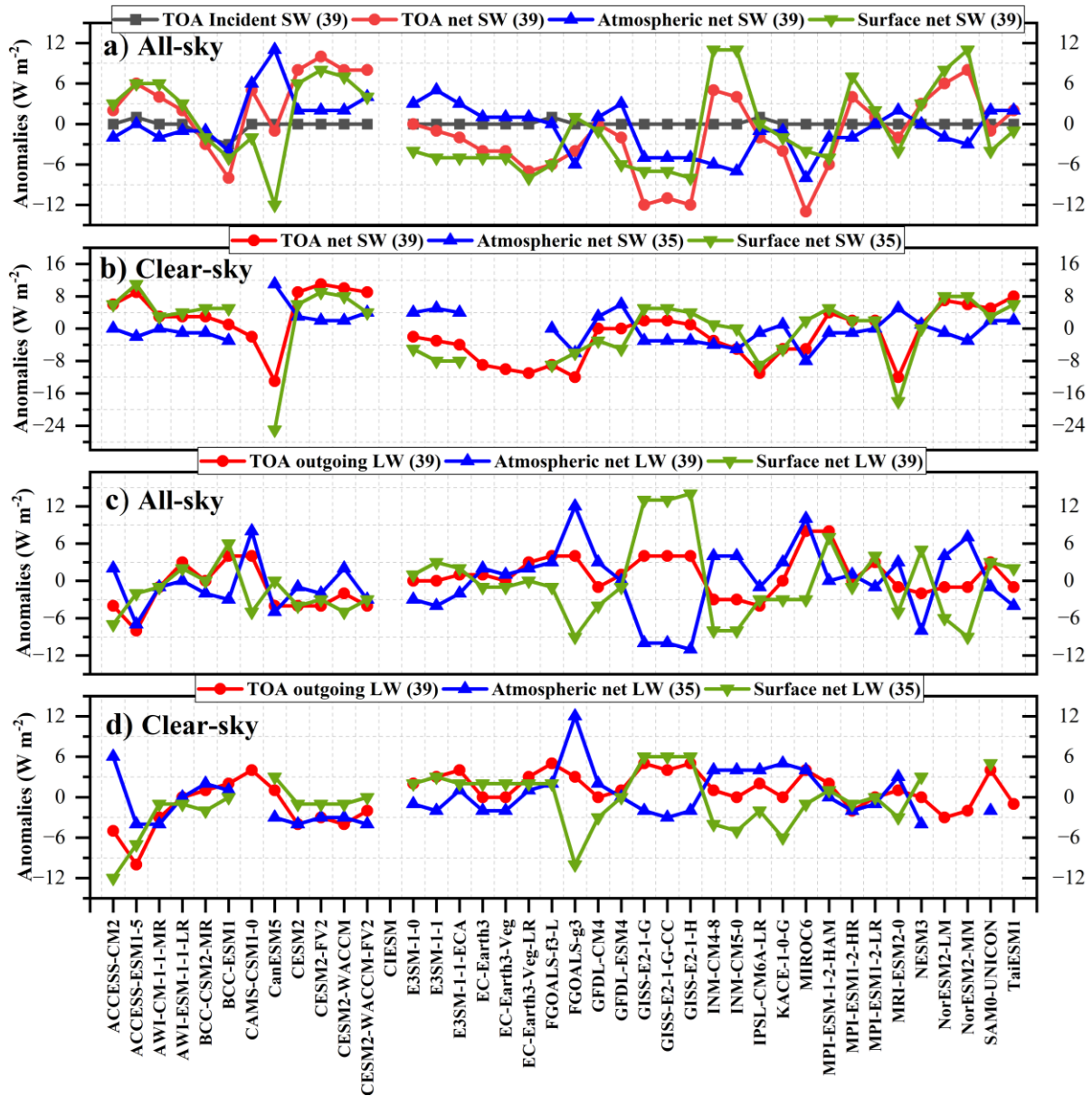
### 172 **3. Assessment of land energy balance budgets under all-sky conditions**

#### 173 3.1. Shortwave components

174 Under all-sky conditions, the present-day annual land-mean anomalies of TOA incident solar radiation  
175 as well as the SW net radiation at the TOA, within the atmosphere, and at the surface regarding to their  
176 respective multi-model means as simulated by various CMIP6 models over East Asia are shown in Fig. 1a.  
177 A summary of the CMIP6 model statistics (such as available model number, model spread, and the standard  
178 deviation (SD)), along with the corresponding multi-model mean, ERA5-, and CERES-derived estimates of  
179 different energy balance components are listed in Table 1. As shown in Fig. 1a, with the exception of the  
180 BCC-CSM2-MR and BCC-CESM1 models, all models give an estimate around  $334 \text{ W m}^{-2}$  for TOA  
181 incoming solar radiation with a very small SD of 0.2, closely matching the multi-model mean as well as the  
182 CERES and ERA5 estimates (Table 1). The multi-model means of solar absorption at the TOA, within the  
183 atmosphere, and at the surface are 217, 73, and  $144 \text{ W m}^{-2}$ , respectively, all within  $2 \text{ W m}^{-2}$  of the biases  
184 against the CERES-derived estimates, while they are 3–4  $\text{W m}^{-2}$  larger for those from ERA5 at the TOA and  
185 within the atmosphere, yielding  $1 \text{ W m}^{-2}$  of bias against the CERES-based estimate at the surface (Table 1).  
186 However, the individual models vary significantly in their simulated annual East Asian land-mean solar  
187 absorption both at the TOA and surface (Fig. 1a), with SDs of around  $6 \text{ W m}^{-2}$  and inter-model spreads of  
188 more than  $20 \text{ W m}^{-2}$  (Table 1). Considering the smaller absolute amount of atmospheric and surface solar  
189 absorption compared to the TOA counterpart (73 and 144 vs.  $217 \text{ W m}^{-2}$ ; Table 1), the relative (percentage)  
190 differences relative to their respective multi-model means (relative (percentage) difference =  
191  $\frac{\text{range}}{\text{multi-model mean}} \times 100\%$ ) indicate that the uncertainties within the atmosphere and at the surface are larger  
192 than that at the TOA (i.e., TOA:  $\frac{22}{217} \times 100\% = 10\%$ ; Atmosphere:  $\frac{19}{73} \times 100\% = 26\%$ ; Surface:  
193  $\frac{23}{144} \times 100\% = 16\%$ ).

194





195

196 **Figure 1.** Annual land mean anomalies of (a, b) shortwave (SW) and (c, d) longwave (LW) budgets  
 197 (Units:  $W m^{-2}$ ) with regard to their respective multi-model means for present-day climate under (a, c)  
 198 all-sky and (b, d) clear-sky conditions over East Asia as simulated by various CMIP6 models. The black, red,  
 199 blue, and green lines represent the TOA incoming solar radiation, as well as the net SW/LW radiation at  
 200 the TOA, within the atmosphere, and at the surface, respectively.

201

202 **Table 1.** Annual land mean estimates (Units:  $W m^{-2}$ ) of the magnitudes of various energy balance  
 203 components and cloud radiative effects (CREs) over East Asia under all-sky and clear-sky conditions at the  
 204 TOA, within the atmosphere, and at the surface, respectively. The CMIP6 model statistics (e.g., available  
 205 model number, spread, standard deviation (SD)), as well as the corresponding multi-model mean, ERA5-,  
 206 and CERES-derived estimates are also given in the Table.

Component ( $W m^{-2}$ )	CMIP6				ERA5	CERES
	models	spread	SD	mean		
<b>TOA</b>						
Solar down	39	4	0.2	334	334	334
Solar up all-sky	39	23	6	-117	-115	-118

Solar net all-sky	39	22	6.1	217	219	216
Solar up clear-sky	39	24	7	-76	-78	-72
Solar net clear-sky	39	24	6.9	258	256	262
SW CRE	39	26	6.5	-41	-37	-46
Thermal up all-sky	39	12	3.5	-224	-225	-226
Thermal up clear-sky	39	15	3.2	-247	-246	-250
LW CRE	39	12	2.4	23	21	24
Net CRE	39	24	5.8	-18	-16	-22
<b>Atmosphere</b>						
SW absorption all-sky	39	19	3.8	73	78	74
SW absorption clear-sky	35	19	3.8	69	77	71
SW CRE	32	33	6.9	4	2	3
LW net all-sky	39	22	5.1	-152	-150	-157
LW net clear-sky	35	16	3.6	-151	-151	-154
LW CRE	32	14	3.3	-2	1	-3
Net CRE	32	35	7.8	1	2	0
<b>Surface</b>						
SW down all-sky	39	33	7.6	186	191	178
SW up all-sky	39	24	6.5	-43	-50	-36
SW absorbed all-sky	39	23	6.1	144	141	142
SW down clear-sky	35	25	4.6	242	238	236
SW up clear-sky	35	27	6.8	-53	-59	-45
SW absorbed clear-sky	32	36	7.8	189	179	191
SW CRE	35	28	6.6	-46	-38	-49
LW down all-sky	39	27	7.9	280	273	285
LW up all-sky	39	23	7.1	-352	-347	-354
LW net all-sky	39	23	5.7	-71	-74	-69
LW down clear-sky	35	26	6.8	256	253	256
LW up clear-sky	35	23	7.1	-351	-347	-353
LW net clear-sky	35	18	4.1	-95	-94	-97
LW CRE	35	12	3.5	24	20	27
net CRE	32	31	6	-21	-18	-22
net radiation	39	20	5.3	72	67	73
LH	40	26	4.7	-43	-38	—
SH	40	21	5.2	-31	-29	—

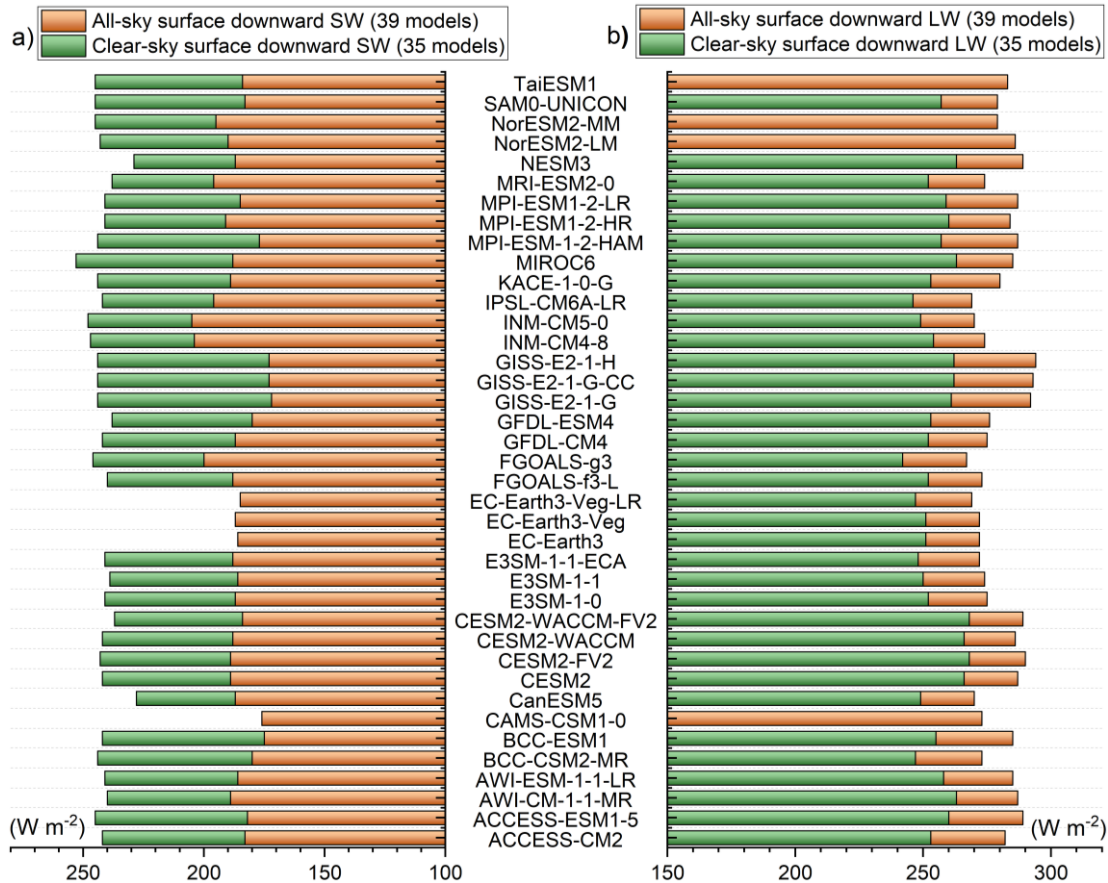
207

208 The simulated SSR, however, shows the largest spread of more than 30 W m<sup>-2</sup> (ranging from 172–205  
209 W m<sup>-2</sup>) among all the substantially differing all-sky surface radiation components, with a large SD of 7.6 W  
210 m<sup>-2</sup> (Fig. 2a; Table 1). The multi-model mean SSR is estimated to be 186 W m<sup>-2</sup>, suggesting positive and  
211 negative deviations of 8 and 5 W m<sup>-2</sup> from the CERES- and ERA5- derived estimates, respectively (Table  
212 1). Interestingly, although the discrepancy between them is very large (8 or 5 W m<sup>-2</sup>), both the resulting  
213 surface solar absorption differences are very small (within 3 W m<sup>-2</sup>), indicating that a higher SSR goes



214 together with a higher surface albedo (Table 1), which agrees well with that on a global mean level (Wild et  
 215 al., 2015).

216



217

218 **Figure 2.** Annual land mean surface downward (a) SW and (b) LW radiation (Units:  $W m^{-2}$ ) under both  
 219 all-sky (orange bars) and clear-sky (green bars) conditions over East Asia as calculated by various CMIP6  
 220 models.

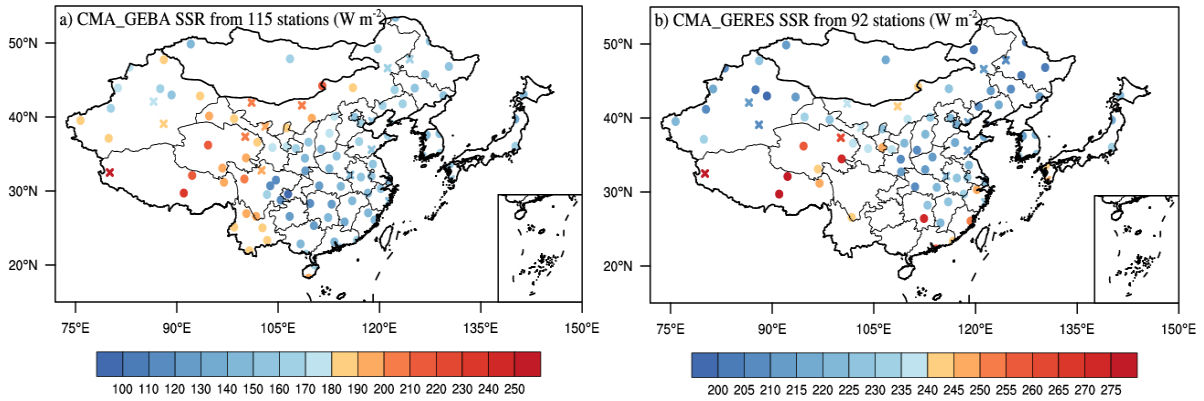
221

222 3.2. Best estimates for the surface downward SW radiation

223 As a major component of Earth’s energy balance, the solar radiation reaching the Earth’s surface  
 224 governs a wide range of surface physical and chemical processes. The spatial distributions of the site-based  
 225 annual mean SSR from the CMA and GEBA (Section 2.1) over East Asia under all-sky conditions are  
 226 presented in Fig. 3a, together with the classified rural and urban sites. In short, the high values are mainly  
 227 located at the high elevation stations over western China and a few island sites in Japan (e.g.,  
 228 Minamitorishima, Japan; not shown in the figure), especially over the TP, with the largest value reaching  
 229  $263 W m^{-2}$  (Geer, Tibet), which is associated with the high atmospheric transparency over these regions.  
 230 However, the low annual mean values are primary over southwestern China, with the smallest value of 103  
 231  $W m^{-2}$  (Shapingba, Chongqing), which is possibly caused by the higher aerosol loadings (Liao et al., 2015;

232 de Leeuw et al., 2018) and more clouds (Li et al., 2017; You et al., 2019; Lei et al., 2020; Zhang et al., 2020)  
233 over these regions. This distribution pattern is highly consistent with that over China documented by Q.  
234 Wang et al. (2021).

235



236

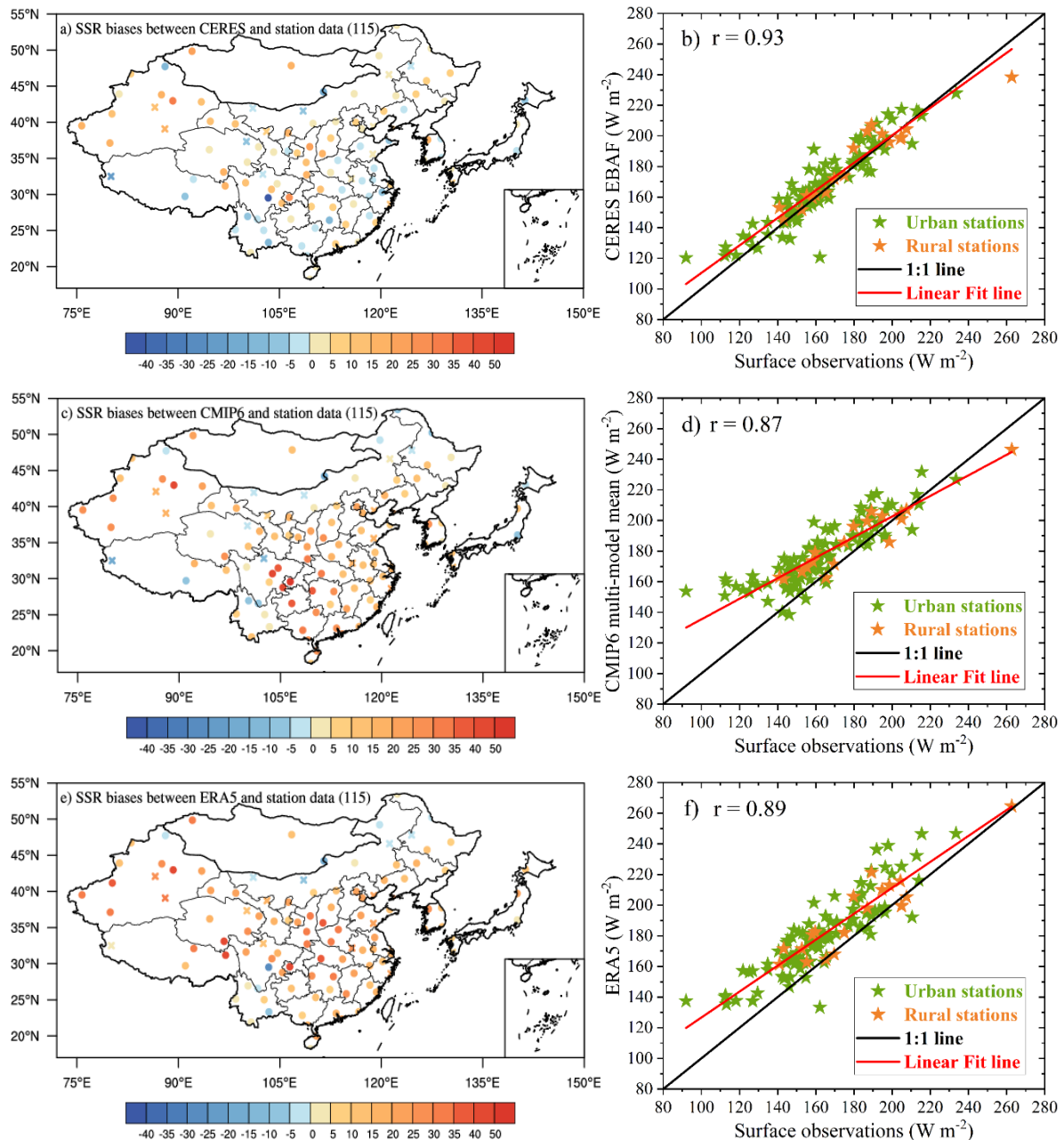
237 **Figure 3.** Spatial distributions of annual mean surface downward solar radiation (SSR) (Units:  $W m^{-2}$ ) under  
238 (a) all-sky and (b) clear-sky conditions over East Asia. The all-sky sites are available from 99 CMA (China)  
239 and 16 GEBA (remaining regions outside China and one site in Hongkong, China) stations, while there are  
240 76 CMA and 16 CERES-interpolated sites for clear-sky conditions. The cross and circle symbols indicate  
241 rural (19 vs. 18 for all-sky and clear-sky conditions) and urban stations (96 vs. 74), respectively.

242

243 Figure 4 shows the distributions of annual mean SSR biases derived from the CERES, CMIP6 multi-  
244 model mean, and ERA5 against the surface observations, as well as the comparisons of their respective  
245 annual land means at the surface sites with their observed counterparts. The corresponding quantifications  
246 of the magnitudes of station-mean biases are also given in Table 2. According to the comparisons, they all  
247 correlate well with the ground-based observations, with their respective high correlation coefficients of 0.93,  
248 0.87, and 0.89, indicative of the highest accuracy in the CERES-derived estimate (Figs. 4b, d, and f). To  
249 quantify their SSR mean biases against the corresponding observed counterparts, the CERES-based bias at  
250 all sites is the smallest, with a station-mean bias of  $3.8 W m^{-2}$ , followed by the CMIP6 multi-model mean  
251 and the ERA5 reanalysis (with respective station-mean biases of 13.8 and  $16.5 W m^{-2}$ ) (Table 2).  
252 Additionally, among all the aforementioned SSR estimates, the East Asian urban sites are in general more  
253 significantly overestimated than the rural sites on average compared to the surface observations (Figs. 4b, d,  
254 and f; Table 2). This further supports the argument that rural stations might be more representative for larger  
255 scale comparisons (e.g., the general circulation model grid scales) than the urban stations (which are  
256 vulnerable to local pollution) (Wang et al., 2018). The overestimations are mainly located in the high-latitude  
257 regions over East Asia for CERES-derived estimates (among them the underestimations mostly from rural  
258 sites), while the underestimates are primarily located in lower-latitude and eastern coastal regions (Figs. 4a  
259 and b). The CMIP6 multi-model mean and ERA5-derived SSR generally greatly overestimate the surface-  
260 based observations both at urban and rural sites, except for the regions over northern and northeastern Inner  
261 Mongolia, northwestern Heilongjiang (located in the northeastern China), and some individual sites over  
262 southwestern China (Figs. 4c-f). The annual land-mean area-weighted average SSR over East Asia derived

263 from CERES is estimated to be  $178 \text{ W m}^{-2}$ , which is closest to the surface observational estimate of  $174 \text{ W m}^{-2}$   
 264  $\text{m}^{-2}$ , compared to the much higher overestimations of both the CMIP6 multi-model mean and ERA5 ( $186$   
 265 and  $191 \text{ W m}^{-2}$ ) against the surface observations (Table 3), which shows a high consistency with their bias  
 266 distributions and the collocated quantifications (Fig. 4; Table 2).

267



268

269 **Figure 4.** Spatial distributions of annual mean SSR biases (Units:  $\text{W m}^{-2}$ ) derived from (a) CERES-EBAF,  
 270 (c) CMIP6 multi-model mean, and (e) ERA5 reanalysis at a combination of the CMA and GEBA sites under  
 271 all-sky conditions over East Asia. The corresponding comparisons of their respective annual means at the  
 272 surface sites with their observed counterparts are displayed in (b), (d), and (f), respectively. The cross and  
 273 circle symbols in Figs. a, c, e as well as the orange and green stars in Figs. b, d, f indicate rural and urban  
 274 stations, respectively.

275

276 **Table 2.** Annual station-mean SSR biases (Units:  $\text{W m}^{-2}$ ) derived from CERES-EBAF, CMIP6 multi-model  
 277 mean, and ERA5 compared to the surface observational sites under all-sky and clear-sky conditions during  
 278 2010-2014 over East Asian land, together with the separate station averages of biases at urban and rural sites.  
 279 The largest percentages of SSR biases relative to their respective station-mean averages are estimated to be  
 280 around 10% and 4% for all-sky and clear-sky conditions.

Station-mean SSR biases against surface sites (Units: $\text{W m}^{-2}$ )	All-sky			Clear-sky		
	all	urban	rural	all	urban	rural
CERES-EBAF - surface sites	3.8	4.2	1.6	0.4	0.5	-0.3
CMIP6 - surface sites	13.8	15.0	7.4	9.1	9.7	6.4
ERA5 - surface sites	16.5	17.2	12.7	5.7	6.2	3.6

281

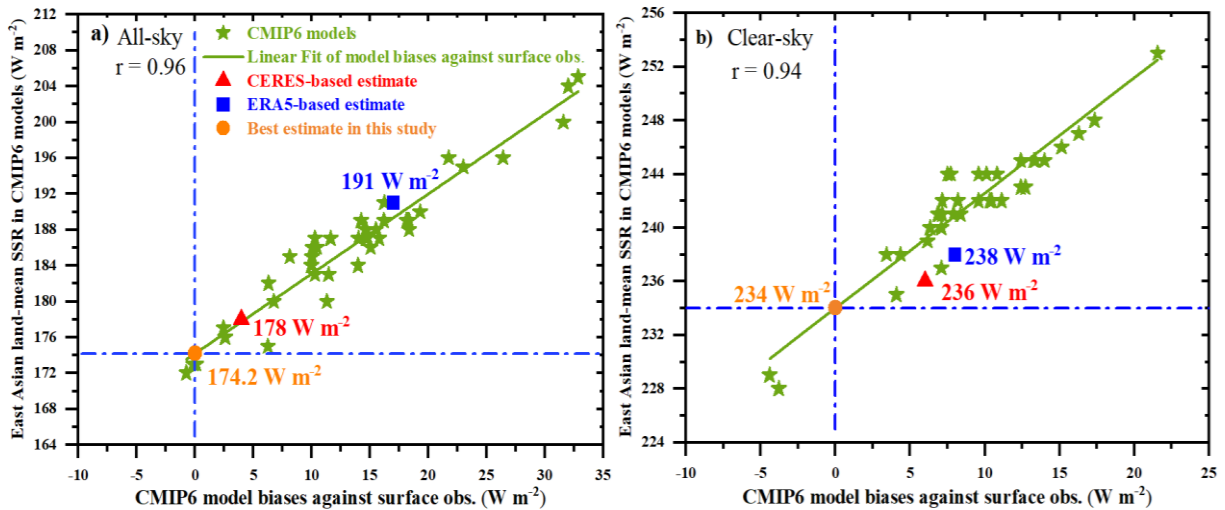
282 **Table 3.** Annual land mean area-weighted average SSR (Units:  $\text{W m}^{-2}$ ) from a combination of the CMA and  
 283 GEBA (CERES-interpolated) site observations under all-sky (clear-sky) conditions during the period 2010-  
 284 2014 over East Asia, together with the corresponding estimates from the CERES-EBAF, CMIP6 multi-  
 285 model means, and ERA5, respectively.

Average annual mean SSR during 2010-2014 over East Asia (Units: $\text{W m}^{-2}$ )	Surface observations	CERES-EBAF	CMIP6	ERA5
All-sky	174	178	186	191
Clear-sky	230	236	242	238

286

287 However, the ground-based observations are spatially limited with sparse stations in some remote  
 288 regions and are thus inadequate for many applications, as they may be not representative for real situations.  
 289 To better constrain the large spread in the model-based SSR outlined above, we combine the ground-based  
 290 observations to obtain the best estimate referring to the approach introduced in (Wild et al., 2013a). Figure  
 291 5a gives various CMIP6 model biases of all-sky SSR at all the surface sites and their respective East Asian  
 292 land means. The higher overestimations relative to surface observations generally correspond to higher  
 293 model-based East Asian land means, with a much higher correlation coefficient of 0.96 than that of 0.88 on  
 294 the global scale (Wild et al., 2015). Thus, the best estimate of the annual East Asian land-mean SSR is  
 295 deduced to be  $174.2 \pm 1.3 \text{ W m}^{-2}$  ( $2\sigma$  uncertainty) in light of the linear regression analysis. The corresponding  
 296 estimates from CERES and ERA5 are also labeled in the figure, at 178 and 191  $\text{W m}^{-2}$ , respectively, implying  
 297 a slight and substantial overestimation for CERES and ERA5 estimates. There is an overall tendency that  
 298 most models overestimate the surface downward SW fluxes (36 out of 39 sites) compared to the ground-  
 299 based observations, with a multi-model mean overestimation relative to site observations of  $13.8 \text{ W m}^{-2}$ ,  
 300 which is also a longstanding issue in climate modelling (Wild et al., 1995; Wild et al., 2015).

301



302

303 **Figure 5.** Annual land mean SSR (Units:  $\text{W m}^{-2}$ ) of various CMIP6 models as well as their respective model  
 304 biases relative to an average over surface sites (99 CMA and 16 GEBA for all-sky; 76 CMA and 16 CERES-  
 305 interpolated sites for clear-sky) under (a) all-sky and (b) clear-sky conditions during 2010-2014 over East  
 306 Asia. Green stars represent various CMIP6 models. Best estimate here (orange circle) can be inferred from  
 307 the intersection between the linear regression line (green solid lines) and the zero-bias line (blue dotted lines).  
 308 Furthermore, the corresponding estimates from CERES-EBAF and ERA5 are also given by red triangle and  
 309 blue square, respectively.

310

### 311 3.3. Longwave components

312 Similar to the all-sky SW counterparts, obvious discrepancies can still be noted in the annual land-mean  
 313 LW radiation over East Asia among models, especially for those within the atmosphere and at the surface  
 314 (Fig. 1c). Correspondingly, the simulated TOA OLR varies in a range of  $12 \text{ W m}^{-2}$ , which is almost  $10 \text{ W}$   
 315  $\text{m}^{-2}$  lower than that within the atmosphere ( $22 \text{ W m}^{-2}$ ) and at the surface ( $23 \text{ W m}^{-2}$ ) (Table 1). The estimated  
 316 annual East Asian land-mean TOA OLR from the CMIP6 multi-model mean is  $-224 \text{ W m}^{-2}$ , within  $2 \text{ W m}^{-2}$   
 317 of the deviations from the CERES- and ERA5-inferred estimates. The model spread of the simulated annual  
 318 land-mean net LW radiation becomes larger from the TOA to the surface, with SDs of 3.5, 5.1, and  $5.7 \text{ W}$   
 319  $\text{m}^{-2}$ , respectively, which shows the same tendency as the relative (percentages) differences with respect to  
 320 their multi-model means (5.4%, 14.5%, and 32.4%).

321 These large discrepancies in surface net LW radiation between models are particularly evident in the  
 322 surface downward LW radiation (Fig. 2b; Table 1), with a range up to  $27 \text{ W m}^{-2}$  (from  $267$  to  $294 \text{ W m}^{-2}$ )  
 323 and a SD of  $7.9 \text{ W m}^{-2}$ , which is also the largest deviation among all components under all-sky conditions.  
 324 Compared to the CERES estimates, the slightly lower surface upward LW radiation ( $-352$  vs.  $-354 \text{ W m}^{-2}$ )  
 325 and much lower surface downward LW radiation ( $280$  vs.  $285 \text{ W m}^{-2}$ ) from the multi-model means are the  
 326 major reason for the small deviation (within  $2 \text{ W m}^{-2}$ ) of the surface net LW radiation between them (Table  
 327 1). It's interesting to note that the annual East Asian land-mean surface upward LW radiation estimated from  
 328 the ERA5 is the lowest among all these estimates, at  $-347 \text{ W m}^{-2}$ , suggesting the lowest surface skin  
 329 temperature of the ERA5 product according to the Stefan-Boltzmann law, followed by the estimates from  
 330 the multi-model mean and CERES (Table 1). In addition, the annual land-mean surface downward LW  
 331 radiation estimated by ERA5 is  $273 \text{ W m}^{-2}$ , approximately 7 and  $12 \text{ W m}^{-2}$  lower than the estimates by the

332 CMIP6 multi-model mean and CERES, respectively (Table 1). Therefore, both the lower surface upward  
333 and downward LW radiation fluxes result in the small deviation in the estimated surface net LW radiation  
334 from ERA5 compared to those from the multi-model mean and CERES (Table 1). Since the reanalysis  
335 products take as many observed atmospheric parameters with global coverage as possible into consideration  
336 during the radiative transfer calculations, they are widely used to obtain more accurate surface LW radiation  
337 (Simmons et al., 2004; Wild et al., 2015). We also examined the corresponding surface LW fluxes from  
338 another reanalysis, namely MERRA-2, and found much lower annual land means than those from ERA5, in  
339 particular for the surface downward LW radiation (not shown), which arrives at the similar conclusions with  
340 that documented by Urraca et al. (2018). Thus, considering the limited observational surface LW radiation  
341 data over East Asia, ERA5 might be the best reference for the estimates of the annual land-mean surface  
342 upward and downward LW radiation, at  $-347$  and  $273 \text{ W m}^{-2}$ , respectively (Table 1).

343

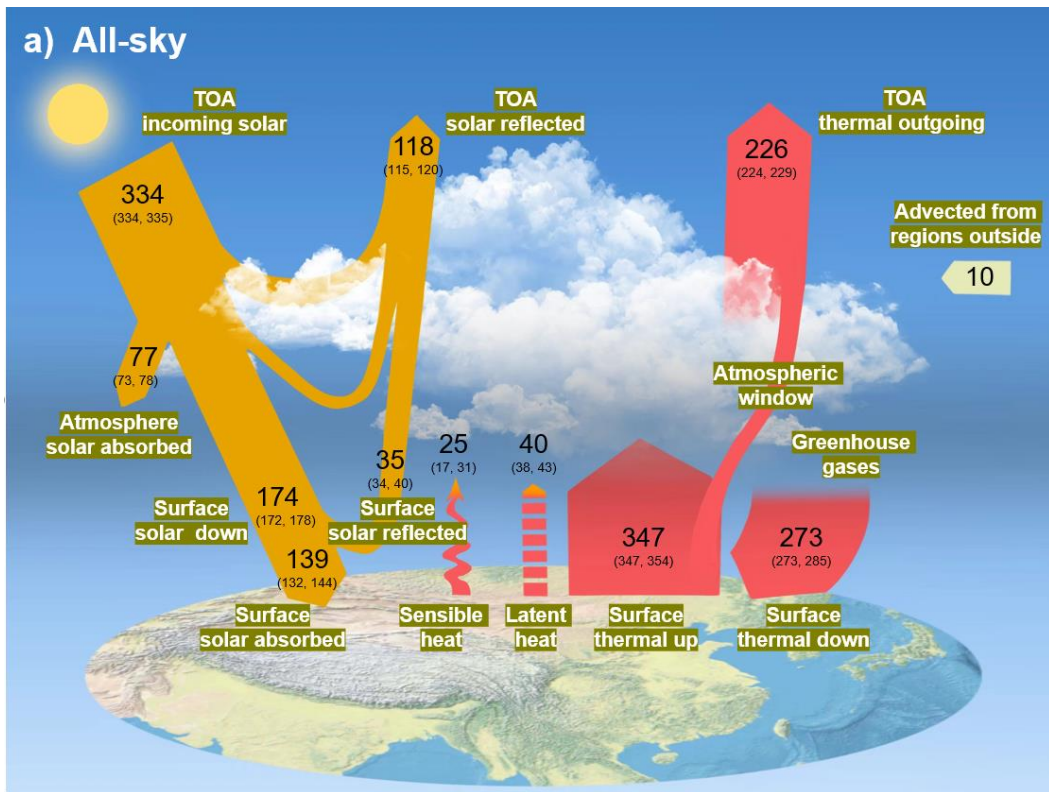
### 344 3.4. Discussion of land energy balance over East Asia under all-sky conditions

#### 345 3.4.1. Radiative components

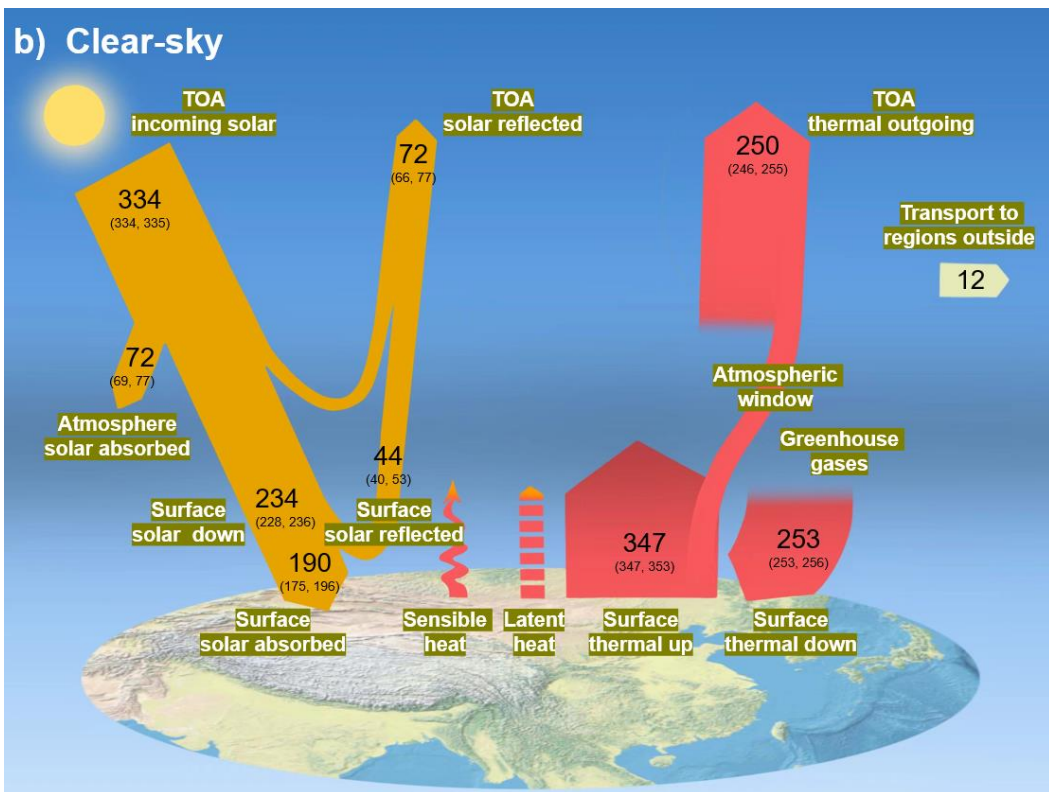
346 Figure 6a displays the schematic diagram of the all-sky land mean energy balance over East Asia,  
347 including the above-mentioned SW and LW radiation budgets and other radiative components discussed in  
348 the following. The estimated annual East Asian land-mean incoming, reflected, and net SW radiation as well  
349 as the OLR at the TOA are therefore  $334$ ,  $-118$ ,  $216$ , and  $-226 \text{ W m}^{-2}$  (Table 1), respectively, based on the  
350 CERES EBAF dataset. The corresponding uncertainties are obtained from the uncertainty of  $2.5$  ( $1\sigma$ )  
351 uncertainty)  $\text{W m}^{-2}$  for both SW and LW fluxes given by (Loeb et al., 2018). The annual East Asian land-  
352 mean TOA OLR in CERES-EBAF is estimated to be  $10 \text{ W m}^{-2}$  larger than the TOA absorbed SW radiation,  
353 implying an energy loss of  $10 \text{ W m}^{-2}$  at the TOA under all-sky conditions, which should be compensated by  
354 the LH and SH transported from regions outside East Asia (Fig. 6a).

355





356



357

358 **Figure 6.** Diagrams of the annual land mean energy balance (Units:  $W m^{-2}$ ) over East Asia under (a) all-  
 359 sky and (b) clear-sky conditions for present-day climate. The uncertainty ranges are also given in  
 360 parentheses.

361



362 For the SSR, the annual East Asian land-mean best estimate based on the CMIP6 multi-model  
363 simulations and surface observations is  $174.2 \text{ W m}^{-2}$  (Fig. 5a and Fig. 6a). Considering the abnormally high  
364 overestimation by ERA5 compared to surface observation, the high value of the uncertainty range is given  
365 by the estimate from CERES EBAF ( $178 \text{ W m}^{-2}$ ), while its low value is from the lowest model estimate ( $172$   
366  $\text{W m}^{-2}$ ; Fig. 2a) (Fig. 6a). The all-sky surface albedo information is derived from the ratio between the  
367 CERES-derived surface upward and downward solar radiation, with a radiation weighted average of around  
368  $0.2$  ( $36.4/178.3$ ) over East Asian land. However, the corresponding surface albedos estimated by the CMIP6  
369 multi-model mean and ERA5 are substantially higher than that from the CERES, with respective averages  
370 of around  $0.23$  ( $42.7/186.4$ ) and  $0.26$  ( $49.6/191$ ). Considering the large spatial coverage of remote sensing  
371 measurement to map albedo globally, the CERES-derived annual East Asian land-mean surface albedo is  
372 adopted as the best estimate in this study. Therefore, considering the rounded best SSR estimate of  $174 \text{ W}$   
373  $\text{m}^{-2}$ , the calculated surface reflected and absorbed SW radiation fluxes are around  $-35$  and  $139 \text{ W m}^{-2}$ ,  
374 respectively. As shown in Table 1, the uncertainty range of the surface absorbed SW radiation is  $132$ – $144$   
375  $\text{W m}^{-2}$  according to the lowest value of CMIP6 models and the highest estimate among the aforementioned  
376 estimates, which gives rise to an uncertainty range of the surface reflected solar radiation of  $34$ – $40 \text{ W m}^{-2}$ .  
377 Together with the annual East Asian land-mean SW absorption at the TOA and surface of  $216$  and  $139 \text{ W}$   
378  $\text{m}^{-2}$ , the best estimate for the atmospheric SW absorption is therefore to be  $77 \text{ W m}^{-2}$ , which is within  $4 \text{ W}$   
379  $\text{m}^{-2}$  of the differences between those estimated from the CMIP6 multi-model mean and CERES and closes  
380 to the ERA5-derived estimate of  $78 \text{ W m}^{-2}$  (Table 1). The uncertainty range of the atmospheric SW  
381 absorption is also determined by the estimates from different data sources as shown in Fig. 6a.

382 The downward LW radiation emitted by the atmosphere is mainly sensitive to the near-surface  
383 temperature, water vapor, and cloud properties, while the surface emission is in proportion to the skin  
384 temperature according to the Stefan-Boltzmann law. As analyzed in section 3.3, the best estimates of the  
385 East Asian annual land-mean surface upward and downward LW radiation amount to  $-347$  and  $273 \text{ W m}^{-2}$ ,  
386 respectively, with uncertainty ranges coming also from the above-discussed different data sources (Fig. 6a).  
387 The surface net LW radiation is then estimated to be  $-74 \text{ W m}^{-2}$  based on the surface upward and downward  
388 LW radiation outlined above. Combined with TOA outgoing thermal radiation of  $-226 \text{ W m}^{-2}$ , the estimated  
389 atmospheric net LW radiation is  $-152 \text{ W m}^{-2}$ , which is close to the collocated estimates from the multi-model  
390 mean ( $-152 \text{ W m}^{-2}$ ) and ERA5 ( $-150 \text{ W m}^{-2}$ ) but deviates substantially from the CERES-derived estimate of  
391  $-157 \text{ W m}^{-2}$  (Table 1). Considering the surface absorbed SW radiation of  $139 \text{ W m}^{-2}$ , a best estimate for  
392 surface net radiation is  $65 \text{ W m}^{-2}$ , suggesting that around  $65 \text{ W m}^{-2}$  of energy is available for the non-radiative  
393 SH and LH. Besides, the ERA5 estimate of  $67 \text{ W m}^{-2}$  is very close to the best estimate of  $65 \text{ W m}^{-2}$ , while  
394 much higher estimates of  $72$  and  $73 \text{ W m}^{-2}$  are obtained from the multi-model mean and CERES (Table 1),  
395 respectively.

396

### 397 3.4.2. Nonradiative components

398 The surface net radiation is mainly balanced by the non-radiative components of SH and LH in addition  
399 to a very small proportion of ground heat flux and melt (less than 1%) (Ohmura, 2004). However, due to the  
400 lack of constraints from in-situ and space observations, this partitioning of the surface net radiation into SH  
401 and LH is still subject to considerable uncertainties. As shown in Fig. S2, the simulated annual East Asian  
402 land-mean LH and SH vary greatly between different models, with a range of 26 and 21 W m<sup>-2</sup>, respectively,  
403 as well as the relative discrepancies relative to their respective multi-model means of 60% ( $\frac{26}{43} \times 100\%$ ) and  
404 68% ( $\frac{21}{31} \times 100\%$ ), respectively, showing larger discrepancies between models with larger uncertainties in SH  
405 (Table 1). The best SH estimate can therefore be obtained from the residual of the LH. To obtain a more  
406 accurate surface LH from available datasets of the multi-model mean and ERA5, we take an average of them  
407 as the best estimate, namely -40 W m<sup>-2</sup>, the uncertainty ranges of which are also given according to these  
408 estimates (Fig. 6a). Note that all the values in this study are calculated on the basis of one decimal point,  
409 which may result in 1 W m<sup>-2</sup> of bias during the rounding process. Combined with the surface net radiation  
410 and LH of 65 and -40 W m<sup>-2</sup>, respectively, the surface SH is estimated to be -25 W m<sup>-2</sup>, the uncertainty range  
411 of which is also given by the existing estimates from various CMIP6 models and ERA5 (Fig. 6a). In addition,  
412 although the annual land-mean SH estimated from the MERRA-2 is much higher than the estimates from  
413 multi-model mean and ERA5 (not shown), the estimated LH is around -39 W m<sup>-2</sup> (not shown), very close to  
414 the best estimate of -40 W m<sup>-2</sup>, which increases our confidence in the estimation of this quantity.

415

### 416 3.4.3. Comparisons with global annual land-mean estimates

417 Notable discrepancies exist in the global land-mean energy budgets reported by Wild et al. (2015) and  
418 the regional land-mean estimates over East Asia in this study (Fig. S3; Table 4). For the SW budgets, the  
419 estimated annual land-mean TOA incident solar radiation over East Asia is 9 W m<sup>-2</sup> higher than that over  
420 global land (334 vs. 325 W m<sup>-2</sup>), implying a slightly lower land-mean solar zenith angle over East Asia.  
421 Comparisons also show a slightly higher relative percentage of TOA reflected solar radiation of 0.8% despite  
422 of the much lower surface reflected SW radiation of 4.3% over East Asian land compared to global land with  
423 respect to their respective TOA incident solar radiation (thereafter call 'relative percentage' for short). This  
424 suggests much more relative atmospheric SW reflection of 5.2% over East Asian land, which agrees fairly  
425 well with more aerosols (Wei et al., 2019) and clouds (King et al., 2013; Fan et al., 2018; also see Fig. S4)  
426 over this region compared to global land. However, the annual land-mean solar radiation reaching the East  
427 Asian surface is around 10 W m<sup>-2</sup> lower than that over global land (174 vs. 184 W m<sup>-2</sup>), approximately  
428 accounting for 52.1% and 56.6% of their respective incident solar radiation at the TOA, respectively,  
429 indicating lower fraction of solar energy arriving at the East Asian surface compared to global land. Together  
430 with the lower annual land-mean surface albedo over East Asian land compared to global land (20% vs.  
431 26%), this leads to the similar relative percentages of surface absorptions (41.6% vs. 41.9%). Although the  
432 magnitude of the atmospheric SW absorptions over East Asian and global land are nearly the same (both  
433 around 77 W m<sup>-2</sup>), the corresponding relative percentage over East Asian land is a little bit lower than that

434 over global land (around 0.6%). This is somewhat unexpected due to the fact of more clouds and aerosol  
 435 loadings over East Asian land, which is possibly offset by the lower water vapor contents caused by the  
 436 higher altitudes and thinner air over the TP.

437

438 **Table 4.** Comparisons of the annual mean SW/LW energy balance components (Units:  $W m^{-2}$ ) over East  
 439 Asian land (this study) and global land (Wild et al., 2015) as well as the corresponding relative percentages  
 440 with regard to their respective TOA incident solar radiation/surface LW emissions, along with the relative  
 441 percentage differences between them.

Component	East Asian land		Global land		Percentage difference
	Annual mean	Relative percentage	Annual mean	Relative percentage	
<b>SW budget</b>					
TOA solar down	334	1	325	1	—
TOA solar up	-118	35.3%	-112	34.5%	0.8%
Atmospheric SW absorption	77	23.1%	77	23.7%	-0.6%
Atmospheric SW reflection	-83	24.9%	-64	19.7%	5.2%
Surface solar down	174	52.1%	184	56.6%	-4.5%
Surface solar up	-35	10.5%	-48	14.8%	-4.3%
Surface solar absorption	139	41.6%	136	41.9%	-0.3%
<b>LW budget</b>					
TOA LW up	-226	65.1%	-232	62.4%	2.7%
Atmospheric LW absorption	-152	43.8%	-166	44.6%	-0.8%
surface LW down	273	78.7%	306	82.3%	-3.6%
Surface LW up	-347	1	-372	1	—

442

443 For the LW budgets, the regional surface LW emission over East Asia is estimated to be much lower  
 444 than the global land-mean estimates in Wild et al. (2015) (Fig. S3), which mainly results from the lower  
 445 temperature over the TP induced by high altitudes. The relative percentage of land mean surface downward  
 446 LW radiation with respect to the surface emission over East Asia is about 78.7 %, which is lower than the  
 447 global estimate of 82.3%, corresponding well to a reduction in greenhouse effect and fewer low clouds due  
 448 to the TP (Fig. S4) considering its coverage over East Asian land. Ultimately, a higher percentage of LW  
 449 radiation is emitted to space over East Asian land compared to global land (65.1% vs. 62.4%). Our estimates  
 450 also indicate approximately similar amounts of LH (40 vs. 38  $W m^{-2}$ ) and much lower SH (25 vs. 32  $W m^{-2}$ )  
 451 over East Asia compared to the global land-mean estimates (Fig. S3), which is possibly related to the  
 452 lower East Asian-land surface temperature.

453 In general, as can be concluded from Table 4, although much less surface SW radiation of 4.3% is  
 454 reflected over East Asian land compared to global land, a slightly more SW reflection of 0.8% is estimated  
 455 at the TOA, indicating much larger atmospheric SW reflection of 5.2% due to the stronger scattering from  
 456 aerosols and clouds over East Asian land than global land. However, the SW absorption within the  
 457 atmosphere over East Asian land is 0.6% lower than that over global land despite of the more absorption  
 458 from clouds and aerosols, which is possibly offset by the lower water vapor contents caused by the thinner  
 459 air over the TP. The lower surface temperature, weaker greenhouse effect and fewer low clouds due to the  
 460 high altitudes and the thinner air over the TP in East Asian land are the major reasons for the relative lower

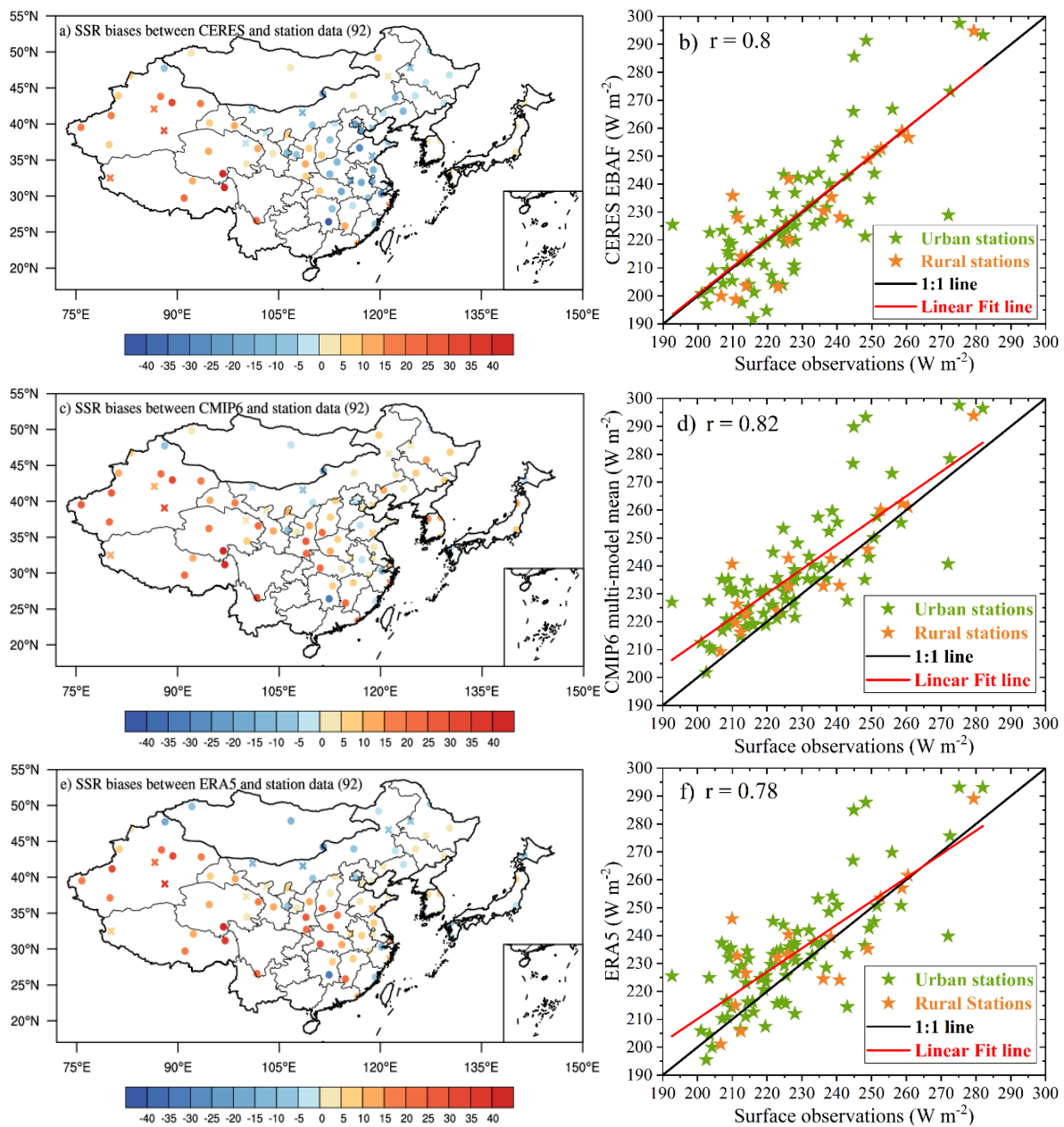
461 surface LW emission, less and more fractions of surface downward LW radiation of 3.6% and the OLR of  
462 2.7% over East Asian land compared to global land, respectively.

463

#### 464 **4. Assessment of land energy balance budgets under clear-sky conditions**

465 The clear-sky land energy balance budgets over East Asia are similarly evaluated as all-sky conditions.  
466 Detailed analyses are given in Supplemental material if interested. The annual land-mean SW clear-sky  
467 absorptions at the TOA and surface over East Asia show larger variations among different models than that  
468 under all-sky conditions (Fig. 1a and b; Table 1), which is consistent with that reported by Wild et al. (2019)  
469 but is amazingly in contrast to the recognition that the representation of clouds is the largest uncertainties in  
470 climate models (Dolinar et al., 2015). Specially, the surface SW clear-sky absorptions simulated by various  
471 models still exhibit a larger uncertainty than the TOA counterparts despite of the lower absolute values (Fig.  
472 1b; Table 1). Contrary to the all-sky counterparts, the simulated clear-sky SSR among different models,  
473 shows notably smaller inter-model spread and SD than the surface SW absorptions (Table 1), with much  
474 smaller model discrepancy compared to the all-sky conditions (Fig. 2a; Table 1).

475 To further constrain the outlined inter-model discrepancy of the simulated clear-sky SSR, surface  
476 observations from the CMA and CERES-interpolated estimates at the GEBA sites are utilized in this study.  
477 The high values of the station-based clear-sky SSR are mainly located in the TP, but with an abnormally  
478 high value located at the southern China (Fig. 3b). All the East Asian land-mean clear-sky SSR estimates  
479 from CERES, CMIP6 multi-model mean, and ERA5 agree reasonably well with the surface observations,  
480 but with smaller correlation coefficients ranging from 0.78 to 0.82 compared to the all-sky conditions (Figs.  
481 7 b, d, and f). The CERES-derived clear-sky SSR is mainly overestimated in central and western China, but  
482 with slight underestimations mainly located in northeastern, eastern, and southern China (Fig. 7a). Similar  
483 bias patterns can also be found in the clear-sky SSR from the CMIP6 multi-model mean and ERA5 compared  
484 to the surface observations, except for some individual sites over northeastern Inner Mongolia, eastern China,  
485 western Mongolia, and Japan (Figs. 7c and e), but with relatively smaller overestimations than the all-sky  
486 counterparts (Figs. 4c and e; Table 2). Specifically, the smallest station mean bias in CERES-derived SSR  
487 compared to the multi-model mean and ERA5 (Table 2) can be attributed to its even distributed surface sites  
488 of overestimations and underestimations (Figs. 7b, d, f). Again, among all the aforementioned clear-sky SSR  
489 biases, more overestimations exist in urban stations than the rural stations (b, d, f in Figs. 4 and 7; Table 2).  
490 Consequently, all East Asian land-mean area-weighted averages of clear-sky SSR from CERES, CMIP6  
491 multi-model mean, and ERA5 show higher overestimations of around 6, 12, and 8  $\text{W m}^{-2}$ , respectively,  
492 compared to the surface observed counterpart of 230  $\text{W m}^{-2}$  (Table 3). Based on the similar method  
493 introduced in Wild et al. (2015), the best estimate for the East Asian land-mean clear-sky SSR is determined  
494 to be  $234 \pm 1.1 \text{ W m}^{-2}$  ( $2\sigma$  uncertainty), with a slightly smaller correlation coefficient of 0.94 and smaller  
495 deviations from the CERES and ERA5 estimates compared to the all-sky counterparts (Fig. 5b; Table 3).  
496 Besides, the overestimations still exist in the observed land-mean clear-sky SSR for most climate models  
497 over East Asia, with a smaller multi-model mean overestimation of 9.1  $\text{W m}^{-2}$  than the all-sky counterparts.



499

500 **Figure 7.** Spatial distributions of annual mean SSR biases derived from (a) CERES-EBAF, (b) CMIP6  
 501 multi-model mean, and (c) ERA5 reanalysis against surface observations from a combination of the CMA  
 502 and CERES-interpolated sites under clear-sky conditions over East Asia. The corresponding comparisons of  
 503 their respective annual land means at the surface sites with their observed counterparts are displayed in (b),  
 504 (d), and (f), respectively. The cross and circle symbols in Figs. a, c, e as well as the orange and green stars  
 505 in Figs. b, d, f indicate rural and urban stations, respectively.

506

507 This clear-sky energy budget only represents the removal of cloud but maintains the same atmospheric  
 508 conditions as the all-sky conditions, which is not balanced because it is not the equilibrium state the Earth  
 509 would achieve when no clouds could form. Ultimately, the clear-sky East Asian land-mean energy budget is  
 510 not closed and with no quantifications of SH and LH as displayed in Fig. 6b. In addition to the analyses  
 511 above, the clear-sky TOA energy budgets are derived from CERES-derived product, with uncertainty ranges

512 referred to Loeb et al. (2018), while the surface LW budgets are again from ERA5 reanalysis. Also,  
 513 additional clear-sky radiation weighted surface albedo of 0.19 from CERES is obtained to estimate the  
 514 surface reflected and absorbed SW radiation. All the uncertainty ranges are given by different data sources  
 515 from various CMIP6 models, as well as the multi-model mean, CERES-, and ERA5-derived estimates,  
 516 except for their TOA counterparts.

517 We doublecheck the energy balance components evaluated in this study by referring to the uncertainty  
 518 ranges from CERES-derived product given by Kato et al. (2018) (Table 5), which indicates that all estimated  
 519 energy components fall within these uncertainty ranges, except for the all-sky surface downward LW  
 520 radiation, with about  $3 \text{ W m}^{-2}$  lower than the corresponding lowest CERES range. This is in line with its  
 521 much higher CERES-derived estimate compared to that of the ERA5 ( $285$  vs.  $273 \text{ W m}^{-2}$ ) (Table 1).

522

523 **Table 5.** Uncertainties (Units:  $\text{W m}^{-2}$ ) in  $1^\circ \times 1^\circ$  regional monthly surface SW, LW, and net (SW + LW)  
 524 fluxes under all-sky and clear-sky conditions for the CERES-EBAF Edition 4.1 product (referring to Kato  
 525 et al. (2018)), as well as its corresponding estimates of various surface fluxes.

Uncertainties( $1\sigma$ )	All-sky	Clear-sky
SW down	$178 \pm 14$	$236 \pm 6$
SW up	$36 \pm 11$	$45 \pm 11$
SW net	$142 \pm 13$	$191 \pm 13$
LW down	$285 \pm 9$	$256 \pm 8$
LW up	$354 \pm 15$	$353 \pm 15$
LW net	$69 \pm 17$	$97 \pm 17$
SW + LW net	$73 \pm 20$	$95 \pm 20$

526

527 Overall, around 21.6% and 56.9% of the TOA incoming solar radiation are absorbed by the atmosphere  
 528 and surface, respectively, for clear-sky conditions, while these absorptions are 23.1% and 41.6% for all-sky  
 529 conditions. This implies that the existence of clouds results in more atmospheric SW absorption of around  
 530 1.5% and much less surface solar absorption of around 15.3% with respect to the TOA incoming solar  
 531 radiation.

532

## 533 5. The cloud radiative effects (CREs)

534 According to the annual land-mean best estimates of radiative components over East Asia under all-sky  
 535 and clear-sky conditions obtained in previous sections, the present-day CREs can be inferred quantitatively  
 536 over this region. The calculated SW, LW, and net CREs at the TOA, within the atmosphere, and at the  
 537 surface are therefore presented in Fig. 8. Moreover, the corresponding calculation formulas are also given in  
 538 the followings:

539

$$540 \text{ TOA SW CRE} = \text{TOA outgoing SW}_{\text{all-sky}} - \text{TOA outgoing SW}_{\text{clear-sky}}$$



541 
$$\text{TOA LW CRE} = \text{TOA outgoing LW}_{\text{all-sky}} - \text{TOA outgoing LW}_{\text{clear-sky}}$$

542 
$$\text{TOA Net CRE} = \text{TOA SW CRE} + \text{TOA LW CRE}$$

543

544 
$$\text{Surface Net SW CRE} = \text{Surface Net SW}_{\text{all-sky}} - \text{Surface Net SW}_{\text{clear-sky}}$$

545 
$$\text{Surface Net LW CRE} = \text{Surface Net LW}_{\text{all-sky}} - \text{Surface Net LW}_{\text{clear-sky}}$$

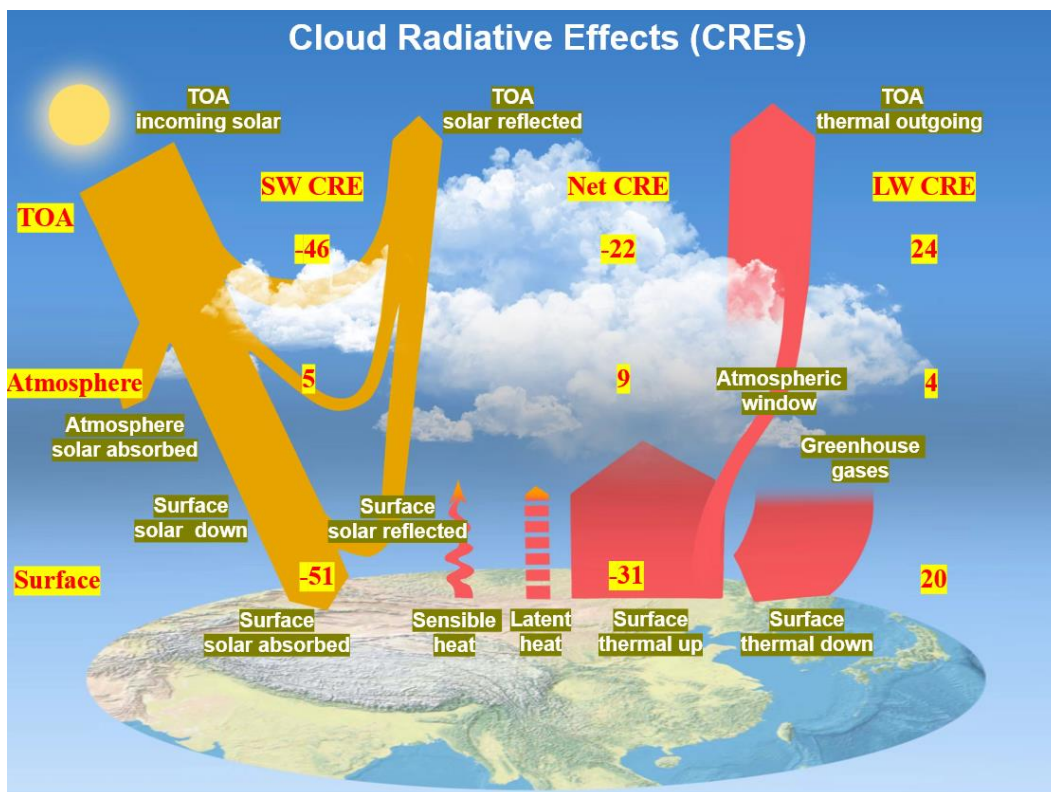
546 
$$\text{Surface Net total CRE} = \text{Surface Net SW CRE} + \text{Surface Net LW CRE}$$

547

548 
$$\text{Atmospheric SW CRE} = \text{TOA SW CRE} - \text{Surface Net SW CRE}$$

549 
$$\text{Atmospheric LW CRE} = \text{TOA LW CRE} - \text{Surface Net LW CRE}$$

550



551

552 **Figure 8.** Diagram of the annual land mean SW, LW, and net (SW + LW) cloud radiative effects (CREs)  
 553 (Units:  $\text{W m}^{-2}$ ) at the TOA, within the atmosphere, and at the surface over East Asia, calculated by the  
 554 differences between all-sky and clear-sky radiation budgets as given in Fig. 7.

555

556 Best estimates for the annual East Asian land-mean reflected solar radiation at the TOA under all-sky  
 557 and clear-sky conditions are  $-118$  and  $-72 \text{ W m}^{-2}$ , respectively, differing by  $-46 \text{ W m}^{-2}$ , indicating that the  
 558 clouds give rise to an extra  $46 \text{ W m}^{-2}$  solar reflection at the TOA, thus cooling the Earth-atmosphere system.

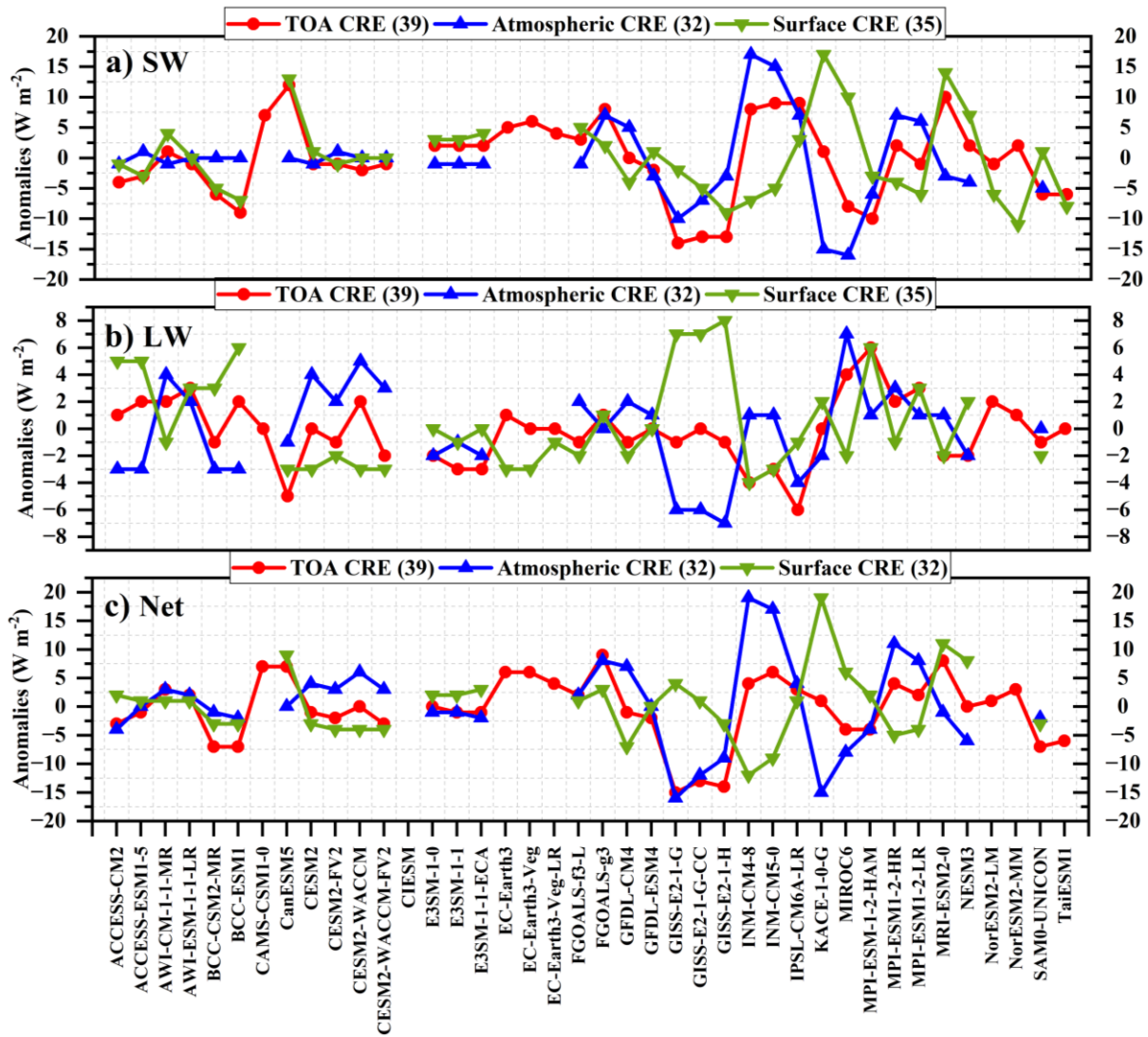


559 Similarly, the TOA LW CRE, obtained as the difference between the TOA thermal radiation under all-sky  
560 and clear-sky conditions, is  $24 \text{ W m}^{-2}$ , suggesting a warming effect of clouds on the system. Thus, the  
561 estimated TOA net CRE is  $-22 \text{ W m}^{-2}$ , pointing out that the overall effects of clouds result in an energy loss  
562 and net cooling to the system, not only in the global mean, but also over East Asian land.

563 At the Earth's surface, the shading effects of clouds are estimated to reduce the surface solar radiation  
564 by  $60 \text{ W m}^{-2}$ , from  $234$  to  $174 \text{ W m}^{-2}$ , while the surface solar absorption differs by  $51 \text{ W m}^{-2}$ , from  $190$  to  
565  $139 \text{ W m}^{-2}$ , namely the surface net SW CRE is  $-51 \text{ W m}^{-2}$ . On cloudy skies, the estimated surface downward  
566 LW radiation increases from  $253$  to  $273 \text{ W m}^{-2}$ , with an increase of  $20 \text{ W m}^{-2}$ , illustrating that the surface  
567 net LW CRE is  $20 \text{ W m}^{-2}$  and therefore leads to a surface warming. Thus, the surface net CRE, i.e., the sum  
568 of the surface net SW and LW CRE, is then  $-31 \text{ W m}^{-2}$ , indicating that clouds contribute more to the SW  
569 energy budgets. Eventually, the clouds lead to the enhancement of the SW and LW absorption within the  
570 atmosphere of around  $5$  and  $4 \text{ W m}^{-2}$ , respectively, thus resulting in an atmospheric net CRE of  $9 \text{ W m}^{-2}$  over  
571 East Asian land.

572 The above CRE estimates are compared to the corresponding estimates from different data sources (Fig.  
573 9; Table 1). Generally, compared to the LW CREs (Fig. 9b), the simulated SW CREs show larger spreads  
574 and SDs amongst models (Fig. 9a; Table 1). For the SW CREs at the TOA, within the atmosphere, and at  
575 the surface, the CERES-derived estimates match perfectly with the best estimates mentioned above, within  
576  $2 \text{ W m}^{-2}$  of the biases, followed by the estimates from the multi-model means and ERA5 (Table 1). For the  
577 LW CREs, the calculated TOA LW CREs from the CMIP6 multi-model mean and CERES differ by no more  
578 than  $1 \text{ W m}^{-2}$  compared to the best estimate, while large differences are noted at the surface LW CREs,  
579 thereby leading to their opposite signs in the atmospheric LW CREs (Fig. 9b; Table 1). Specifically, since  
580 the ERA5-based TOA LW CRE deviates by no more than  $3 \text{ W m}^{-2}$  with the best estimate of  $24 \text{ W m}^{-2}$  with  
581 nearly the same surface LW CRE, the estimated atmospheric LW CRE is therefore the closest to the best  
582 estimate (Table 1). This is owing to the fact that we make use of the ERA5 data as the reference to estimate  
583 the surface LW radiation. Thus, the major reason for the large discrepancies in the atmospheric and surface  
584 LW CREs estimated from different data sources with respect to the best estimates in this study is the  
585 determination of the surface downward and upward LW radiation, which is also the reason for the large  
586 deviations in their net CREs (Fig. 9c).

587



588

589 **Figure 9.** Annual land mean anomalies of (a) SW, (b) LW, and (c) net (SW + LW) CRE (Units: W m<sup>-2</sup>) at  
 590 the TOA (red line), within the atmosphere (blue line), and at the surface (green line) with regard to their  
 591 respective multi-model means over East Asia, respectively, as represented by various CMIP6 models. The  
 592 numbers in the parentheses indicate the available CMIP6 climate models for the corresponding radiation  
 593 components.

594

595 A better comparison with the global annual mean best estimates of CREs by Wild et al. (2019) is given  
 596 in Fig. S5. At the TOA, a slightly lower and much lower East Asian land-mean SW and LW CREs of 1 W  
 597 m<sup>-2</sup> and 4 W m<sup>-2</sup> result in 3 W m<sup>-2</sup> more energy loss at the TOA compared to the globe. At the surface, much  
 598 lower annual East Asian land-mean SW and LW CREs by 3 W m<sup>-2</sup> and 8 W m<sup>-2</sup> are estimated compared to  
 599 the values over the globe, leading to a net CRE deviation of 5 W m<sup>-2</sup>, indicative of 5 W m<sup>-2</sup> more energy loss  
 600 at the surface. However, lower and higher annual East Asian land-mean SW and LW CREs of 2 and 4 W m<sup>-2</sup>  
 601 within the atmosphere contribute to the nearly close net CRE with a deviation of no more than 2 W m<sup>-2</sup>  
 602 compared to the global mean estimates. On the whole, lower annual East Asian land-mean best estimates in  
 603 the absolute values of surface SW and LW CREs as well as the TOA LW CRE compared to their global  
 604 mean counterparts give rise to the CRE differences between them.

## 605 **6. Summary and conclusions**

606 This study aims to explore how the energy budgets are interrupted by the complex orographic and  
607 thermal effects of the TP, as well as the high anthropogenic aerosol emissions over East Asian land compared  
608 to global land, based on complementary data sources from space and surface observations, as well as the  
609 CMIP6 climate models and ERA5 reanalysis. A further quantitative investigation of CREs at the TOA,  
610 within the atmosphere, and at the surface is also conducted.

611 Comparisons between all-sky and clear-sky energy budgets indicate that the overall effects of clouds  
612 greatly reduce the surface solar absorption by about 15.3% and enhance that within the atmosphere by 1.5%.  
613 Compared to the global land energy budget estimates from Wild et al. (2015), for the SW budgets, notably  
614 more atmospheric SW reflection of 5.2% but with a slightly less atmospheric SW absorption of 0.6% with  
615 respect to their respective TOA incident solar radiation are estimated over East Asian land, possibly  
616 indicating that the lower water vapor content effects due to TP overcompensate for the aerosol and cloud  
617 effects over East Asian land. For the LW budgets, a substantially lower surface LW emission of around 25  
618  $\text{W m}^{-2}$  and smaller relative surface downward LW radiation of around 3.6% with respect to their respective  
619 surface emissions can be noticed over East Asian land compared to global land, which possibly result from  
620 the lower regional surface skin temperature, as well as the weaker greenhouse effect and fewer low clouds  
621 mainly induced by the high altitude and thinner air over TP, thus leading to a higher percentage of regional  
622 OLR of 2.7%.

623 The CREs over East Asian land are inferred through the energy budget differences between all-sky and  
624 clear-sky conditions. The clouds reduce the solar absorption at the TOA by  $46 \text{ W m}^{-2}$  and enhance the TOA  
625 thermal radiation by  $24 \text{ W m}^{-2}$ , respectively, leading to a TOA net CRE of  $-22 \text{ W m}^{-2}$ , a more cooling effect  
626 on the regional climate system than that over globe ( $-19 \text{ W m}^{-2}$ ). At the surface, the net CRE is estimated to  
627 be  $-31 \text{ W m}^{-2}$  according to less solar absorption of  $51 \text{ W m}^{-2}$  and more downward thermal radiation of  $20 \text{ W}$   
628  $\text{m}^{-2}$ , indicative of larger cloud impacts on SW radiation. Within the atmosphere, the estimated net CRE is  $9$   
629  $\text{W m}^{-2}$  due to an increase of  $5 \text{ W m}^{-2}$  of solar absorption and  $4 \text{ W m}^{-2}$  of the net thermal radiation, respectively.  
630 Compared to the global mean best estimates of CREs as introduced by Wild et al. (2019), relatively lower  
631 East Asian land-mean best estimates of surface SW and LW CREs as well as the TOA LW CRE contribute  
632 to the CRE differences between them.

633 On the whole, all the estimated land-mean energy balance components over East Asia in this study fall  
634 within the uncertainty ranges of the CERES-derived assessments, except for the all-sky surface downward  
635 LW radiation. More accurate and reliable datasets should be utilized to reduce the substantial uncertainties  
636 in the regional energy balance estimates, particularly in the surface budgets, and more widespread temporal  
637 and spatial representations of energy budget research are recommended for more comprehensive  
638 comparisons in future. For example, newly published surface radiation products with high resolutions based  
639 on satellite datasets (e.g., Letu et al., 2022; Xu et al., 2022) are expected to make sense in improving the  
640 accuracy of the regional/global surface radiation budget studies.

641 *Acknowledgments.* This research was funded by the National Key Research and Development Program of  
642 China (2017YFA0603502) and the Science and Technology Development Fund of CAMS  
643 (2021KJ004&2022KJ019). The Global Energy Balance Archive (GEBA) is co-funded by the Federal  
644 Office of Meteorology and Climatology Meteo Swiss within the framework of GCOS Switzerland.

645

646 *Data Availability.* The CERES SYN1deg data is available at [https://ceres-tool.larc.nasa.gov/ord-](https://ceres-tool.larc.nasa.gov/ord-tool/jsp/SYN1degEd41Selection.jsp)  
647 [tool/jsp/SYN1degEd41Selection.jsp](https://ceres-tool.larc.nasa.gov/ord-tool/jsp/SYN1degEd41Selection.jsp); The AIRS data is accessible from  
648 [https://disc.gsfc.nasa.gov/datasets/AIRS3STM\\_006/summary?keywords=AIRS](https://disc.gsfc.nasa.gov/datasets/AIRS3STM_006/summary?keywords=AIRS); The MODIS data is from  
649 [https://ladsweb.modaps.eosdis.nasa.gov/archive/allData/61/MYD08\\_M3/?process=ftpAsHttp&path=allDat](https://ladsweb.modaps.eosdis.nasa.gov/archive/allData/61/MYD08_M3/?process=ftpAsHttp&path=allData%2f61%2fMYD08_M3)  
650 [a%2f61%2fMYD08\\_M3](https://ladsweb.modaps.eosdis.nasa.gov/archive/allData/61/MYD08_M3/?process=ftpAsHttp&path=allData%2f61%2fMYD08_M3); The CloudSat data is from [http://www.cloudsat.cira.colostate.edu/data-](http://www.cloudsat.cira.colostate.edu/data-products/level-2b/2b-cwc-ro)  
651 [products/level-2b/2b-cwc-ro](http://www.cloudsat.cira.colostate.edu/data-products/level-2b/2b-cwc-ro); The MERRA-2 dataset is obtained at  
652 [https://disc.gsfc.nasa.gov/datasets/M2IMNPANA\\_5.12.4/summary?keywords=merra-2](https://disc.gsfc.nasa.gov/datasets/M2IMNPANA_5.12.4/summary?keywords=merra-2). The ERA-Interim  
653 is from <https://apps.ecmwf.int/datasets/data/interim-full-moda/levtype=sfc>.

654

655 *Author contributions.* HZ, MW, and QW proposed the main ideas of this study. QW designed and wrote the  
656 manuscript. SY provided the homogenized ground-based surface solar radiation data. QC, XZ, and GS  
657 contributed to the interpretation of the results. BX and YW assisted with the figures. All co-authors  
658 participated in discussions and provided constructive suggestions.

659

660 *Competing interests.* The authors declare that they have no conflict of interest.

661

## 662 **References**

- 663 Boeke, R. C., and Taylor, P. C.: Evaluation of the Arctic surface radiation budget in CMIP5 models, *J. Geophys.*  
664 *Res.-Atmos.*, 121, 8525–8548, <https://doi.org/10.1002/2016JD025099>, 2016.
- 665 Christensen, M. W., Behrangi, A., L’Ecuyer, T. S., Wood, N. B., Lebsock, M. D., and Stephens, G. L.: Arctic  
666 observation and reanalysis integrated system: A new data product for validation and climate study, *B. Am.*  
667 *Meteorol. Soc.*, 97, 907–916, <https://doi.org/10.1175/BAMS-D-14-00273.1>, 2016.
- 668 de Leeuw, G., Sogacheva, L., Rodriguez, E., Kourtidis, K., Georgoulias, A. K., Alexandri, G., Amiridis, V.,  
669 Proestakis, E., Marinou, E., Xue, Y., and van der A, R.: Two decades of satellite observations of AOD over  
670 mainland China using ATSR-2, AATSR and MODIS/Terra: data set evaluation and large-scale patterns, *Atmos.*  
671 *Chem. Phys.*, 18, 1573–1592, <https://doi.org/10.5194/acp-18-1573-2018>, 2018.
- 672 Dolinar, E. K., Dong, X., Xi, B., Jiang, J. H., and Su, H.: Evaluation of CMIP5 simulated clouds and TOA  
673 radiation budgets using NASA satellite observations, *Clim. Dynam.*, 44, 2229–2247,  
674 <https://doi.org/10.1007/s00382-014-2158-9>, 2015.
- 675 Eyring, V., Bony, S., Meehl, G. A., Senior, C. A., Stevens, B., Stouffer, R. J., and Taylor, K. E.: Overview of the  
676 Coupled Model Intercomparison Project Phase 6 (CMIP6) experimental design and organization, *Geosci.*  
677 *Model Dev.*, 9, 1937–1958, <https://doi.org/10.5194/gmd-9-1937-2016>, 2016.
- 678 Fan, T., Zhao, C., Dong, X., Liu, X., Yang, X., Zhang, F., Shi, C., Wang, Y., and Wu, F.: Quantify contribution  
679 of aerosol errors to cloud fraction biases in CMIP5 Atmospheric Model Intercomparison Project simulations,  
680 *Int. J. Climatol.*, 38, 3140–3156, <https://doi.org/10.1002/joc.5490>, 2018.
- 681 Fasullo, J. T., and Trenberth, K. E.: The annual cycle of the energy budget. Part I: Global mean and land-ocean  
682 exchanges, *J. Climate*, 21, 2297–2312, <https://doi.org/10.1175/2007JCLI1935.1>, 2008a.
- 683 Fasullo, J. T., and Trenberth, K. E.: The annual cycle of the energy budget. Part II: Meridional structures and  
684 poleward transports, *J. Climate*, 21, 2313–2325, <https://doi.org/10.1175/2007JCLI1936.1>, 2008b.
- 685 Ghan, S. J., Liu, X., Easter, R. C., Zaveri, R., Rasch, P. J., Yoon, J.-H., and Eaton, B.: Toward a minimal

686 representation of aerosols in climate models: Comparative decomposition of aerosol direct, semidirect, and  
687 indirect radiative forcing, *J. Climate*, 25, 6461–6476, <https://doi.org/10.1175/JCLI-D-11-00650.1>, 2012.

688 Gilgen, H., Wild, M., and Ohmura, A.: Means and trends of shortwave irradiance at the surface estimated from  
689 global energy balance archive data, *J. Climate*, 11, 2042–2061, [https://doi.org/10.1175/1520-0442\(1998\)011<2042:MATOSI>2.0.CO;2](https://doi.org/10.1175/1520-0442(1998)011<2042:MATOSI>2.0.CO;2), 1998.

690 He, Y., Wang, K., Zhou, C., and Wild, M.: A revisit of global dimming and brightening based on the sunshine  
691 duration, *Geophys. Res. Lett.*, 45, 4281–4289, <https://doi.org/10.1029/2018GL077424>, 2018.

692 Hersbach, H., Bell, B., Berrisford, P., Hirahara, S., Horányi, A., Muñoz-Sabater, J., Nicolas, J., Peubey, C., Radu,  
693 R., Schepers, D., Simmons, A., Soci, C., Abdalla, S., Abellan, X., Balsamo, G., Bechtold, P., Biavati, G., Bidlot,  
694 J., Bonavita, M., De Chiara, G., Dahlgren, P., Dee, D., Diamantakis, M., Dragani, R., Flemming, J., Forbes,  
695 R., Fuentes, M., Geer, A., Haimberger, L., Healy, S., Hogan, R. J., Hólm, E., Janisková, M., Keeley, S.,  
696 Laloyaux, P., Lopez, P., Lupu, C., Radnoti, G., de Rosnay, P., Rozum, I., Vamborg, F., Villaume, S., and  
697 Thépaut, J.: The ERA5 global reanalysis, *Q. J. Roy. Meteor. Soc.*, 146, 1999–2049,  
698 <https://doi.org/10.1002/qj.3803>, 2020.

699 Huang, G., Li, Z., Li, X., Liang, S., Yang, K., Wang, D., and Zhang, Y.: Estimating surface solar irradiance from  
700 satellites: Past, present, and future perspectives, *Remote Sens. Environ.*, 233, 111371,  
701 <https://doi.org/10.1016/j.rse.2019.111371>, 2019.

702 Kato, S., Rose, F. G., Rutan, D. A., Thorsen, T. J., Loeb, N. G., Doelling, D. R., Huang, X., Smith, W. L., Su, W.,  
703 and Ham, S.: Surface Irradiances of Edition 4.0 Clouds and the Earth’s Radiant Energy System (CERES)  
704 Energy Balanced and Filled (EBAF) data product, *J. Climate*, 31, 4501–4527, <https://doi.org/10.1175/JCLI-D-17-0523.1>, 2018.

705 Kim, B., and Lee, K.: Radiation component calculation and energy budget analysis for the Korean Peninsula  
706 region, *Remote Sens.*, 10, 1147, <https://doi.org/10.3390/rs10071147>, 2018.

707 King, M. D., Platnick, S., Menzel, W. P., Ackerman, S. A., and Hubanks, P. A.: Spatial and temporal distribution  
708 of clouds observed by MODIS onboard the Terra and Aqua satellites, *IEEE T. Geosci. Remote Sens.*, 51, 3826–  
709 3852, <https://doi.org/10.1109/TGRS.2012.2227333>, 2013.

710 L’Ecuyer, T. S., Beaudoin, H. K., Rodell, M., Olson, W., Lin, B., Kato, S., Clayson, C. A., Wood, E., Sheffield,  
711 J., Adler, R., Huffman, G., Bosilovich, M., Gu, G., Robertson, F., Houser, P. R., Chambers, D., Famiglietti, J.  
712 S., Fetzer, E., Liu, W. T., Gao, X., Schlosser, C. A., Clark, E., Lettenmaier, D. P., and Hilburn, K.: The observed  
713 state of the energy budget in the early twenty-first century, *J. Climate*, 28, 8319–8346,  
714 <https://doi.org/10.1175/JCLI-D-14-00556.1>, 2015.

715 Lei, Y., Letu, H., Shang, H., and Shi, J.: Cloud cover over the Tibetan Plateau and eastern China: a comparison  
716 of ERA5 and ERA-Interim with satellite observations, *Clim. Dynam.*, 54, 2941–2957,  
717 <https://doi.org/10.1007/s00382-020-05149-x>, 2020.

718 Letu, H., Nakajima, T. Y., Wang, T., Shang, H., Ma, R., Yang, K., Baran, A. J., Riedi, J., Ishimoto, H., and Yoshida,  
719 M.: A new benchmark for surface radiation products over the East Asia–Pacific region retrieved from the  
720 Himawari-8/AHI next-generation geostationary satellite, *B. Am. Meteorol. Soc.*, 103, E873–E888,  
721 <https://doi.org/10.1175/BAMS-D-20-0148.1>, 2022.

722 Li, J., -L. F., Waliser, D. E., Stephens, G., Lee, S., L’Ecuyer, T., Kato, S., Loeb, N., and Ma, H.: Characterizing  
723 and understanding radiation budget biases in CMIP3/CMIP5 GCMs, contemporary GCM, and reanalysis, *J.*  
724 *Geophys. Res.-Atmos.*, 118, 8166–8184, <https://doi.org/10.1002/jgrd.50378>, 2013.

725 Li, J., and Mao, J.: A preliminary evaluation of global and East Asian cloud radiative effects in reanalyses, *Atmos.*  
726 *and Ocean. Sci. Lett.*, 8, 100–106, <https://doi.org/10.3878/AOSL20140093>, 2015.

727 Li, J., Mao, J., and Wang, F.: Comparative study of five current reanalyses in characterizing total cloud fraction  
728 and top-of-the-atmosphere cloud radiative effects over the Asian monsoon region, *Int. J. Climatol.*, 37, 5047–  
729 5067, <https://doi.org/10.1002/joc.5143>, 2017.

730 Li, Z., Niu, F., Fan, J., Liu, Y., Rosenfeld, D., and Ding, Y.: Long-term impacts of aerosols on the vertical  
731 development of clouds and precipitation, *Nat. Geosci.*, 4, 888–894, <https://doi.org/10.1038/ngeo1313>, 2011.

732 Liao, H., Chang, W., and Yang, Y.: Climatic effects of air pollutants over china: A review, *Adv. Atmos. Sci.*, 32,  
733 115–139, <https://doi.org/10.1007/s00376-014-0013-x>, 2015.

734 Lin, B., Stackhouse Jr., P. W., Minnis, P., Wielicki, B. A., Hu, Y., Sun, W., Fan, T., and Hinkelman, L. M.:  
735 Assessment of global annual atmospheric energy balance from satellite observations, *J. Geophys. Res.-Atmos.*,  
736 113, <https://doi.org/10.1029/2008JD009869>, 2008.

737 Liu, Y., Bao, Q., Duan, A., Qian, Z. A., and Wu, G.: Recent progress in the impact of the Tibetan Plateau on  
738 climate in China, *Adv. Atmos. Sci.*, 24, 1060–1076, <https://doi.org/10.1007/s00376-007-1060-3>, 2007.

739 Loeb, N. G., Doelling, D. R., Wang, H., Su, W., Nguyen, C., Corbett, J. G., Liang, L., Mitrescu, C., Rose, F. G.,  
740 and Kato, S.: Clouds and the Earth’s Radiant Energy System (CERES) Energy Balanced and Filled (EBAF)  
741 Top-of-Atmosphere (TOA) Edition-4.0 data product, *J. Climate*, 31, 895–918, <https://doi.org/10.1175/JCLI-D-17-0208.1>, 2018.

745 Mayer, M., Tietsche, S., Haimberger, L., Tsubouchi, T., Mayer, J., and Zuo, H.: An improved estimate of the  
746 coupled Arctic energy budget, *J. Climate*, 32, 7915–7934, <https://doi.org/10.1175/JCLI-D-19-0233.1>, 2019.

747 Mercado, L. M., Bellouin, N., Sitch, S., Boucher, O., Huntingford, C., Wild, M., and Cox, P. M.: Impact of  
748 changes in diffuse radiation on the global land carbon sink, *Nature*, 458, 1014–1017,  
749 <https://doi.org/10.1038/nature07949>, 2009.

750 Ohmura, A.: Cryosphere During the Twentieth Century, *The state of the planet: frontiers and challenges in*  
751 *geophysics*, *Geophys. Monogr. Ser.*, 150, 239–257, <https://doi.org/10.1029/150gm19>, 2004.

752 Previdi, M., Smith, K. L., and Polvani, L. M.: How well do the CMIP5 models simulate the Antarctic atmospheric  
753 energy budget? *J. Climate*, 28, 7933–7942, <https://doi.org/10.1175/JCLI-D-15-0027.1>, 2015.

754 Raschke, E., Kinne, S., Rossow, W. B., Stackhouse, P. W., and Wild, M.: Comparison of radiative energy flows  
755 in observational datasets and climate modeling, *J. Appl. Meteorol. Clim.*, 55, 93–117,  
756 <https://doi.org/10.1175/JAMC-D-14-0281.1>, 2016.

757 Simmons, A. J., Jones, P. D., Da Costa Bechtold, V., Beljaars, A. C. M., Kållberg, P. W., Saarinen, S., Uppala, S.  
758 M., Viterbo, P., and Wedi, N.: Comparison of trends and low-frequency variability in CRU, ERA-40, and  
759 NCEP/NCAR analyses of surface air temperature, *J. Geophys. Res.-Atmos.*, 109,  
760 <https://doi.org/10.1029/2004JD005306>, 2004.

761 Stephens, G. L.: Cloud feedbacks in the climate system: A critical review, *J. Climate*, 18, 237–273,  
762 <https://doi.org/10.1175/JCLI-3243.1>, 2005.

763 Stephens, G. L., Li, J., Wild, M., Clayson, C. A., Loeb, N., Kato, S., L'Ecuyer, T., Stackhouse, P. W., Lebsock,  
764 M., and Andrews, T.: An update on Earth's energy balance in light of the latest global observations, *Nat. Geosci.*,  
765 5, 691–696, <https://doi.org/10.1038/ngeo1580>, 2012.

766 Tang, W. J., Yang, K., Qin, J., Cheng, C. C. K., and He, J.: Solar radiation trend across China in recent decades:  
767 a revisit with quality-controlled data, *Atmos. Chem. Phys.*, 11, 393–406, [https://doi.org/10.5194/acp-11-393-](https://doi.org/10.5194/acp-11-393-2011)  
768 2011, 2011.

769 Thomas, C. M., Dong, B., and Haines, K.: Inverse modeling of global and regional energy and water cycle fluxes  
770 using earth observation data, *J. Climate*, 33, 1707–1723, <https://doi.org/10.1175/JCLI-D-19-0343.1>, 2020.

771 Trenberth, K. E., Fasullo, J. T., and Balmaseda, M. A.: Earth's energy imbalance, *J. Climate*, 27, 3129–3144,  
772 <https://doi.org/10.1175/JCLI-D-13-00294.1>, 2014.

773 Trenberth, K. E., Fasullo, J. T., and Kiehl, J.: Earth's global energy budget, *B. Am. Meteorol. Soc.*, 90, 311–324,  
774 <https://doi.org/10.1175/2008BAMS2634.1>, 2009.

775 Trolliet, M., Walawender, J. P., Bourlès, B., Boilley, A., Trentmann, J., Blanc, P., Lefèvre, M., and Wald, L.:  
776 Downwelling surface solar irradiance in the tropical Atlantic Ocean: a comparison of re-analyses and satellite-  
777 derived data sets to PIRATA measurements, *Ocean Sci.*, 14, 1021–1056, [https://doi.org/10.5194/os-14-1021-](https://doi.org/10.5194/os-14-1021-2018)  
778 2018, 2018.

779 Urraca, R., Huld, T., Gracia-Amillo, A., Martinez-de-Pison, F. J., Kaspar, F., and Sanz-Garcia, A.: Evaluation of  
780 global horizontal irradiance estimates from ERA5 and COSMO-REA6 reanalyses using ground and satellite-  
781 based data, *Sol. Energy*, 164, 339–354, <https://doi.org/10.1016/j.solener.2018.02.059>, 2018.

782 Wang, H., Zhang, H., Xie, B., Jing, X., He, J., and Liu, Y.: Evaluating the Impacts of Cloud Microphysical and  
783 Overlap Parameters on Simulated Clouds in Global Climate Models, *Adv. Atmos. Sci.*,  
784 <https://doi.org/10.1007/s00376-021-0369-7>, 2021.

785 Wang, K.: Measurement biases explain discrepancies between the observed and simulated decadal variability of  
786 surface incident solar radiation, *Sci. Rep.*, 4, 6144, <https://doi.org/10.1038/srep06144>, 2014.

787 Wang, K., Ma, Q., Li, Z., and Wang, J.: Decadal variability of surface incident solar radiation over China:  
788 Observations, satellite retrievals, and reanalyses, *J. Geophys. Res.-Atmos.*, 120, 6500–6514,  
789 <https://doi.org/10.1002/2015JD023420>, 2015.

790 Wang, Q., Zhang, H., Yang, S., Chen, Q., Zhou, X., Shi, G., Cheng, Y., and Wild, M.: Potential driving factors  
791 on surface solar radiation trends over China in recent years, *Remote Sens.*, 13, 704,  
792 <https://doi.org/10.3390/rs13040704>, 2021.

793 Wang, Y., Trentmann, J., Yuan, W., and Wild, M.: Validation of CM SAF CLARA-A2 and SARA-E surface  
794 solar radiation datasets over China, *Remote Sens.*, 10, 1977, <https://doi.org/10.3390/rs10121977>, 2018.

795 Wang, Y., Wild, M., Sanchez-Lorenzo, A., and Manara, V.: Urbanization effect on trends in sunshine duration in  
796 China, *Ann. Geophys.*, 35, 839–851, <https://doi.org/10.5194/angeo-35-839-2017>, 2017.

797 Wang, Y., and Wild, M.: A new look at solar dimming and brightening in China, *Geophys. Res. Lett.*, 43, 11,  
798 711–777, 785, <https://doi.org/10.1002/2016GL071009>, 2016.

799 Wei, J., Peng, Y., Guo, J., and Sun, L.: Performance of MODIS Collection 6.1 Level 3 aerosol products in spatial-  
800 temporal variations over land, *Atmos. Environ.*, 206, 30–44, <https://doi.org/10.1016/j.atmosenv.2019.03.001>,  
801 2019.

802 Wild, M.: Progress and challenges in the estimation of the global energy balance, *AIP Conference Proceedings*,  
803 1810, 20004, <https://doi.org/10.1063/1.4975500>, 2017a.

804 Wild, M.: Towards global estimates of the surface energy budget, *Curr. Clim. Change Rep.*, 3, 87–97,  
805 <https://doi.org/10.1007/s40641-017-0058-x>, 2017b.

806 Wild, M.: The global energy balance as represented in CMIP6 climate models, *Clim. Dynam.*, 55, 553–577,  
807 <https://doi.org/10.1007/s00382-020-05282-7>, 2020.

808 Wild, M., Folini, D., Hakuba, M. Z., Schär, C., Seneviratne, S. I., Kato, S., Rutan, D., Ammann, C., Wood, E. F.,  
809 and König-Langlo, G.: The energy balance over land and oceans: an assessment based on direct observations  
810 and CMIP5 climate models, *Clim. Dynam.*, 44, 3393–3429, <https://doi.org/10.1007/s00382-014-2430-z>, 2015.

811 Wild, M., Folini, D., Schär, C., Loeb, N., Dutton, E. G., and König-Langlo, G.: The global energy balance from  
812 a surface perspective, *Clim. Dynam.*, 40, 3107–3134, <https://doi.org/10.1007/s00382-012-1569-8>, 2013a.

813 Wild, M., Folini, D., Schär, C., Loeb, N., Dutton, E. G., and König-Langlo, G.: A new diagram of the global  
814 energy balance, *AIP Conference Proceedings*, 1531, 628–631, <https://doi.org/10.1063/1.4804848>, 2013b.

815 Wild, M., Grieser, J., and Schär, C.: Combined surface solar brightening and increasing greenhouse effect support  
816 recent intensification of the global land-based hydrological cycle, *Geophys. Res. Lett.*, 35,  
817 <https://doi.org/10.1029/2008GL034842>, 2008.

818 Wild, M., Hakuba, M. Z., Folini, D., Dörig-Ott, P., Schär, C., Kato, S., and Long, C. N.: The cloud-free global  
819 energy balance and inferred cloud radiative effects: an assessment based on direct observations and climate  
820 models, *Clim. Dynam.*, 52, 4787–4812, <https://doi.org/10.1007/s00382-018-4413-y>, 2019.

821 Wild, M., Hakuba, M. Z., Folini, D., Schär, C., and Long, C.: New estimates of the Earth radiation budget under  
822 cloud-free conditions and cloud radiative effects, *AIP Conference Proceedings*, 1810, 90012,  
823 <https://doi.org/10.1063/1.4975552>, 2017.

824 Wild, M., Ohmura, A., Gilgen, H., and Roeckner, E.: Validation of general circulation model radiative fluxes  
825 using surface observations, *J. Climate*, 8, 1309–1324, [https://doi.org/10.1175/1520-0442\(1995\)008<1309:VOGCMR>2.0.CO;2](https://doi.org/10.1175/1520-0442(1995)008<1309:VOGCMR>2.0.CO;2), 1995.

826 Wu, G., Duan, A., Liu, Y., Mao, J., Ren, R., Bao, Q., He, B., Liu, B., and Hu, W.: Tibetan Plateau climate  
827 dynamics: recent research progress and outlook, *Natl. Sci. Rev.*, 2, 100–116,  
828 <https://doi.org/10.1093/nsr/nwu045>, 2015.

829 Xu, J., Liang, S., and Jiang, B.: A global long-term (1981–2019) daily land surface radiation budget product from  
830 AVHRR satellite data using a residual convolutional neural network, *Earth Syst. Sci. Data*, 14, 2315–2341,  
831 <https://doi.org/10.5194/essd-14-2315-2022>, 2022.

832 Xu, X., Lu, C., Shi, X., and Gao, S.: World water tower: An atmospheric perspective, *Geophys. Res. Lett.*, 35,  
833 <https://doi.org/10.1029/2008GL035867>, 2008a.

834 Xu, X., Zhang, R., Koike, T., Lu, C., Shi, X., Zhang, S., Bian, L., Cheng, X., Li, P., and Ding, G.: A new integrated  
835 observational system over the Tibetan Plateau, *B. Am. Meteorol. Soc.*, 89, 1492–1496, 2008b.

836 Yang, S., Wang, X. L., and Wild, M.: Homogenization and trend analysis of the 1958–2016 in situ surface solar  
837 radiation records in China, *J. Climate*, 31, 4529–4541, <https://doi.org/10.1175/JCLI-D-17-0891.1>, 2018.

838 Yang, S., Wang, X. L., and Wild, M.: Causes of dimming and brightening in China inferred from homogenized  
839 daily clear-sky and all-sky in situ surface solar radiation records (1958–2016), *J. Climate*, 32, 5901–5913,  
840 <https://doi.org/10.1175/JCLI-D-18-0666.1>, 2019.

841 You, Q., Liu, J., and Pepin, N.: Changes of summer cloud water content in China from ERA-Interim reanalysis,  
842 *Global Planet. Change*, 175, 201–210, <https://doi.org/10.1016/j.gloplacha.2019.02.014>, 2019.

843 Zhang, H., Zhao, M., Chen, Q., Wang, Q., Zhao, S., Zhou, X., and Peng, J.: Water and ice cloud optical thickness  
844 changes and radiative effects in East Asia, *J. Quant. Spectrosc. Radiat. Transf.*, 254, 107213,  
845 <https://doi.org/10.1016/j.jqsrt.2020.107213>, 2020.

846  
847